the anterior PSM is not required for normal R-C polarity patterning. To elucidate this issue further, we focused on the expression of *Mesp2*, which is thought to be the final output signal of the segmentation clock. *Mesp2* is initially expressed over one somite length and then becomes localized in the rostral compartment (Takahashi et al., 2000). This dynamic expression pattern generates a gradient of Mesp2 activity that allows PSM cells to form the R-C pattern within a somite (Takahashi et al., 2003; Takahashi et al., 2000). We therefore next compared the *Mesp2* expression pattern at the cellular level among the wild-type, $Lfng^{-/-}$ and $Hes7{>}Lfng/Lfng^{-/-}$ embryos using high-resolution in situ hybridization. By focusing on the length of the *Mesp2* transcription domain along the A-P axis, we found four distinct patterns in the wild-type embryos: (1) no signal (n=4/15); (2) most cells show nuclear dots indicating transcriptional initiation, and the length of the *Mesp2* transcription domain is approximately 11-13 cells (Fig. 4G; n=3/15); (3) active stage in which signals can be observed in the cytoplasm in addition to nuclear dots, and the length of *Mesp2* transcription is approximately 10-12 cells, with anterior cells showing stronger signals (Fig. 4H; n=5/15); and (4) rostral localization in which the length of the *Mesp2* transcription domain becomes approximately 5-6 cells (Fig. 4I; n=3/15). In contrast to wild-type embryos, only one pattern was observed in the *Lfng*-null embryos: signals were observed in the cytoplasm in addition to nuclear dots, the expression levels were randomized for each cells, and the length of the *Mesp2* transcription domain was approximately 9-11 cells (Fig. 4J; n=11/11). These results indicate that *Mesp2* expression is always present in the anterior PSM without clear on/off cycles in the *Lfng*-null embryo. In addition, the *Mesp2* expression domain is kept to one somite length and there is no clear localization into the rostral compartment, although cellular or cell cluster-level localization might occur in a salt-and-pepper pattern in the absence of Lfng. Importantly, the *Mesp2* expression pattern was found to show four distinct patterns similar to those in wild-type embryos even in the $Hes7{>}Lfng/Lfng^{-/-}$ embryos, i.e. no signal (1/9), transcriptional initiation (Fig. 4K, n=2/9), active stage (Fig. 4L, n=3/9) and rostral localization (Fig. 4M; n=3/9). Our findings thus indicate that the oscillation of cNICD alone is sufficient to generate the normal *Mesp2* expression pattern and that the anterior PSM-specific regulation of cNICD via Lfng is dispensable for this process.

Modeling of the *Mesp2* expression pattern

To test the validity of our above hypothesis, we performed computer simulations. Our model is based on that previously proposed by Lewis and colleagues, in which the oscillatory waves emanate, travel and eventually cease, as it adopts the notion of maturity, which delays the oscillation cycle towards the anterior as time proceeds (Palmeirim et al., 1997). In this model of Lewis, the cessation of the oscillatory waves triggers periodic gene expression along an anterior-posterior direction that leads to the formation of the somites (Palmeirim et al., 1997). In our current study, we applied the Lewis model to the oscillatory waves of the cNICD and assumed Fgf as a molecular basis for maturity. We further incorporated the regulatory network required for *Mesp2* expression, in which cNICD oscillation and Tbx6 synergistically activate (Yasuhiko et al., 2006; Oginuma et al., 2008), whereas the Fgf gradient suppresses *Mesp2* expression and Tbx6 is degraded downstream of Mesp2 (Fig. 5A). Very surprisingly, this simple simulation successfully mimicked some specific features of dynamic *Mesp2* transcription (red line), not only in terms of on/off cycles but also with regard to temporal changes in the expression pattern (from one somite length to rostral localization) along the anterior-posterior axis (Fig. 5B; see Movie 1 in the supplementary material), similar to that observed in vivo (Fig. 4G-I; see Fig. S3A,B in the supplementary material). In addition, this simulation also reproduced the gradient of Mesp2 activity accumulation (black line), which is similar to the *Mesp2*-β-gal pattern we observed in the $Mesp2^{lacZ/+}$ embryos (see Fig. S3E in the supplementary material).

To test the importance of the cNICD wave for the gradient formation of Mesp2 activity, we examined *Mesp2* expression under constant activity of cNICD in the PSM (Fig. 5C; see Movie 2 in the supplementary material). In this instance, *Mesp2* expression is always observed in the anterior PSM without either clear on/off cycles or localization at the rostral compartment, which is very similar to the in vivo situation of the $Lfng^{-/-}$ embryos (Fig. 4J; see Fig. S3C,D,F in the supplementary material). Interestingly, in our model, neither the formation of the waved pattern of cNICD nor its migration is necessary to establish the gradient of Mesp2 activity because a spatially uniform, but temporally oscillating, Notch signaling activity is sufficient to reproduce this gradient (see Fig. S4 and Movie 3 in the supplementary material). Without a traveling wave, however, the temporal transition of the Mesp2 expression pattern from a one-somite length to a rostral localization was not reproduced (see Fig. S4 and Movie 3 in the supplementary material). We thus speculate that this transition might be important for robust somite formation with a correct R-C polarity and propose that the wave of Notch activity enables PSM cells to establish not only the periodic expression of *Mesp2*, but also their localization into the rostral compartment. Our model therefore provides a new concept that indicates that a progressive oscillating wave of Notch activity is translated into the R-C polarity of a somite through the regulation of the Mesp2 expression pattern.

Anterior PSM-specific *Lfng* cannot rescue the defects in *Mesp2*-null or *Lfng*-null mice

Finally, to further ask the significance of the anterior striped cNICD domain for somite boundary formation, we established a mouse line that reproduces this expression pattern by introducing *Lfng* cDNA at the *Mesp2* locus using embryonic stem cell-mediated homologous recombination (see Fig. S1E in the supplementary material). The resulting heterozygous mice showed no abnormalities and we generated an intercross of $Mesp2^{Lfng/+}$ to yield $Mesp2^{Lfng/Lfng}$. In the $Mesp2^{Lfng/Lfng}$ embryos, cNICD signals were suppressed in the *Lfng*-expressing cells in the anterior PSM (Fig. 6B), as seen in the wild type (Fig. 6A). We further found that some of the cells that did not express *Lfng* maintained cNICD signals, indicating that Lfng suppresses cNICD production in a cell-autonomous manner (Fig. 6D). However, Lfng did not rescue the phenotype of the *Mesp2*-null mice (Fig. 6H-M), indicating that the function of *Lfng* downstream of *Mesp2* is not important.

We next introduced this transgene into the *Lfng*-null genetic background to generate a $Mesp2^{Lfng/+}Lfng^{-/-}$ mouse. The expression levels of *Lfng* in the *Mesp2* locus were found to be low (Fig. 6C,E; see Fig. S5C in the supplementary material), but we did observe downregulation of the cNICD signal in the *Mesp2*-expressing cells (Fig. 6F) in comparison with the *Lfng*-null embryos (Fig. 6G). Furthermore, *Hes5* expression (see Fig. S5D in the supplementary material), a target gene of Notch signaling, was severely downregulated in both the $Mesp2^{Lfng/Lfng}$ and $Mesp2^{Lfng/+}Lfng^{-/-}$ embryos (see Fig. S5F,H in the supplementary material) compared with *Mesp2*- and *Lfng*-null embryos (see Fig. S5E,G in the supplementary material), indicating that *Lfng* under the control of *Mesp2* might effectively suppress Notch signaling. However, we did

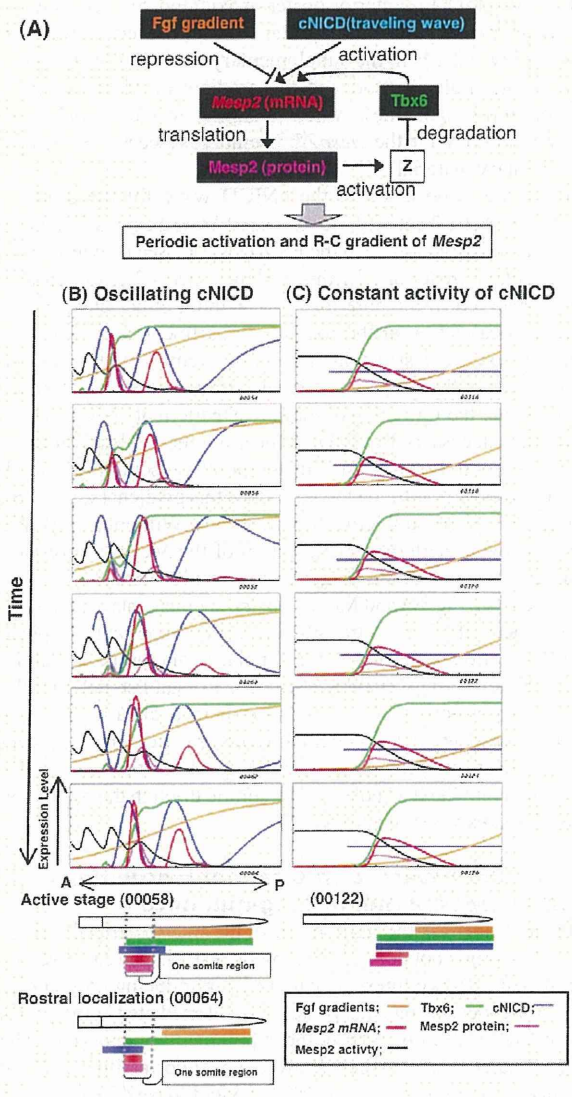

Fig. 5. Model of *Mesp2* expression. (**A**) Schematic representation indicating relationships among *Mesp2* mRNA, Mesp2 protein, Tbx6, cNICD and Fgf signaling, which is used for computer simulation to reproduce the periodic activation and R-C gradient of *Mesp2* expression. z is a hypothetical molecule that functions downstream of Mesp2 and mediates negative-feedback regulation of Tbx6. (**B**,**C**) Expression patterns of *Mesp2*, cNICD and other proteins along the anteroposterior axis predicted in our numerical model. Snapshot images of computer simulations of one cycle of somite formation in the presence (B) or absence (C) of cNICD oscillation are shown. Colored lines indicate levels of cNICD (blue), Fgf8 (orange), *Mesp2* expression (mRNA, red line; protein, pink line) and Tbx6 (green). Mesp2 activity, reflecting the total accumulation of Mesp2 protein, is shown as a tracking line in black. Data sets were taken from Movies 1 (frame 54-64) and 2 (frame 116-126) in the supplementary material, respectively. cNICD (blue) was made to disappear in the panels after one somite is formed, according to experimental observations (Morimoto et al., 2005; Oginuma et al., 2008). Lower diagrams indicate the relationships among these factors at critical time points. Snapshot (00058) corresponds to the transcriptionally active stage of *Mesp2* in which a cNICD wave (blue) reaches the anterior PSM and *Mesp2* (red) is activated in the one-somite region. Snapshot (00064) corresponds to the rostral localization stage, i.e. following the anterior shift of the cNICD wave, the *Mesp2* expression domain also shifts to the rostral region, generating a gradient of Mesp2 activity (black). As the level of cNICD is constant in the *Lfng*-null situation [corresponding to snapshot (00112)], *Mesp2* expression (red) does not show a dynamic pattern and regresses posteriorly.

not detect any significant rescue of the segmental morphology in the developing embryos or of the vertebral morphology at any level along the anteroposterior axis in the $Mesp2^{Lfng/+}Lfng^{-/-}$ mice compared with the *Lfng*-null mouse (Fig. 6N-Q; see Fig. S6 in the supplementary material). These results further confirmed that the suppression of cNICD signaling by stabilized Lfng is not sufficient for normal somitogenesis to occur.

DISCUSSION

The requirement for Notch signaling during mouse somitogenesis

In our current study, we reveal that the cNICD on/off state is not required for somite boundary formation during somitogenesis in the mouse. Consistent with this, recent studies in zebrafish embryos suggest that the function of Notch signaling is only to synchronize the oscillations among PSM cells, and that this pathway has no other function during segmentation (Riedel-Kruse et al., 2007; Horikawa et al., 2006; Ozbudak and Lewis, 2008). However, we propose from our current data that Notch signaling has a crucial function also as an output of the segmentation clock during mouse development.

This contention is supported by earlier evidence that *Mesp2* expression is severely downregulated in the absence of Notch signaling (Barrantes et al., 1999; Takahashi et al., 2000). Moreover, it has been shown that constitutive activation of Notch signaling in the paraxial mesoderm induces *Mesp2* transcription without clear on/off cycles (Feller et al., 2008) and it is also evident from other reports that Notch signaling is crucial for the establishment of R-C patterning of somites in the mouse (Takahashi et al., 2000; Takahashi et al., 2003; Feller et al., 2008). These results together suggest that the function of Notch signaling is not only to synchronize oscillations but that Notch acts also as an important output signal of the segmentation clock, at least in mouse somitogenesis. We thus speculate that Notch signaling is a key factor that mediates the transduction of clock activities into the morphological segmental pattern by regulating *Mesp2* expression. However, it is known that several oscillating components in Notch, Wnt and Fgf signaling pathways are coordinated to generate the segmentation clock network in mice. Hence, *Mesp2* transcription might not be regulated by Notch signaling alone and several pathways might govern the spatiotemporal pattern of *Mesp2* expression. The coordination of these complex networks might well be fundamental to normal somitogenesis.

A new model for the establishment of R-C polarity during somitogenesis

Based on our present findings, we propose a new function for oscillating Notch signaling, which is translated into the R-C polarity of a somite via the regulation of *Mesp2* expression in the anterior PSM. Previous models have proposed that the establishment of R-C polarity requires cell-cell communication (Takahashi et al., 2003; Dale and Pourquie, 2000), whereas we propose a model in which a

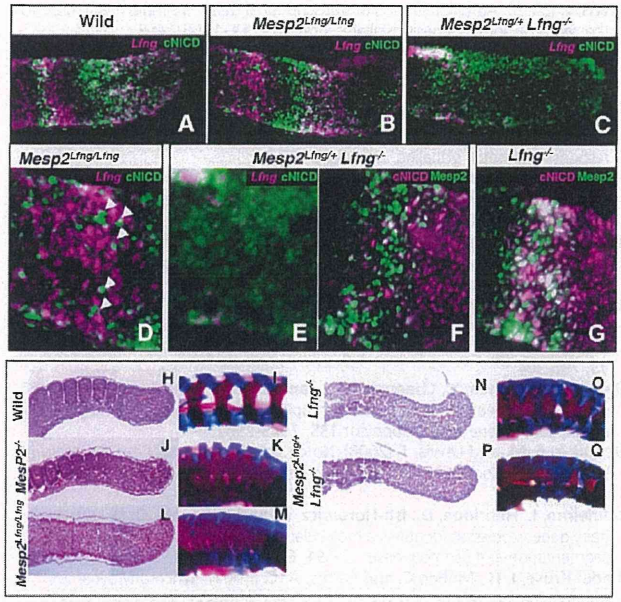

Fig. 6. Exogenous *Lfng* under the control of the *Mesp2* promoter does not rescue the phenotype of the *Mesp2*$^{-/-}$ or *Lfng*$^{-/-}$ mouse. (**A-G**) Sections of E11.5 embryos double stained for *Lfng* mRNA and cNICD (A-E) or for Mesp2 and cNICD (F,G). Higher magnification images of B and C are shown in D and E, respectively. In the *Mesp2*$^{Lfng/Lfng}$ embryo, cNICD formation (B,D, *n*=3) is suppressed in the anterior PSM. The arrowheads in D indicate *Lfng* non-expressing cells that maintain cNICD formation cell-autonomously. In the *Mesp2*$^{Lfng/+}$*Lfng*$^{-/-}$ embryos, cNICD (F, *n*=5) is effectively suppressed in the Mesp2-expressing cells compared with *Lfng*-null embryos (G, *n*=6). (**H-Q**) Comparison of the segmental morphologies in the E11.5 embryonic tail region (H,J,L,N,P) and E17.5 vertebral region (I,K,M,O,Q) among the different genotypes indicated. Neither the *Mesp2*$^{Lfng/Lfng}$ (L,M) nor *Mesp2*$^{Lfng/+}$*Lfng*$^{-/-}$ (P,Q) mice show any recovery of the *Mesp2*$^{-/-}$ (J,K) or *Lfng*$^{-/-}$ (N,O) phenotypes. Number of samples: H, *n*=4; I, *n*=6; J, *n*=3; K, *n*=4; L, *n*=3; M, *n*=6; N, *n*=3; O, *n*=6; P, *n*=3; Q, *n*=7.

cell-autonomous mechanism utilizes Notch signaling oscillation in the posterior PSM. This notion is further supported by computer simulations, in which we found that an appropriate translation of spatiotemporal information provided by the traveling wave of cNICD is sufficient to create the dynamic *Mesp2* expression pattern, i.e. on/off cycles and rostral localization (Fig. 5B; see Movie 1 in the supplementary material). In these simulation experiments, the generation of the traveling wave was based on the earlier work of Lewis (Palmeirim et al., 1997), and the translation of the wave information into *Mesp2* expression was modeled on the gene network that we elucidated previously (Oginuma et al., 2008; Yasuhiko et al., 2006). In the model, the cNICD wave, an activator of *Mesp2*, travels from the posterior to the anterior, whereas the levels of Fgf, a repressor of *Mesp2*, are higher toward the posterior. Consequently, as a single wave passes through a nascent somite, the net transcriptional activation of *Mesp2*, which reflects the amount of cNICD subtracted by the amount of Fgf, is higher toward the rostral part of the presumptive somite. The resulting gradient of Mesp2 activity might thus allow PSM cells to establish a rostral identity and the segmental border. Hence, this is the first model to demonstrate that R-C polarity in the somite is generated as a direct output of the segmentation clock.

The repression of Tbx6, an activator of *Mesp2*, downstream of Mesp2 is another important component in our model. This regulatory module prevents *Mesp2* expression after one traveling wave of cNICD has passed, and thus fixes the R-C gradient pattern of Mesp2. The next wave of Notch signaling cannot affect the Mesp2 pattern created by the former wave. To reproduce the intensive degradation of Tbx6 at anterior regions, we had to adjust the parameters for Tbx6 degradation. We did not need to change any of the other standard parameters we initially chose, suggesting that the qualitative features of the model are not so sensitive to the quantitative values of the parameters. In our simulation analysis, however, we did not reproduce the sharp anterior boundaries of Tbx6 and Mesp2 accumulation (green and black lines, respectively, in Fig. 5B; see Movie 1 in the supplementary material) that have been observed in vivo. To create a sharp boundary of Tbx6 and Mesp2, which should be required to create a fine segmentation boundary, further adjustment of the parameters or another mechanism might be required. In this regard, the next important challenge will be to investigate the molecular basis of the sharpening expression boundaries of Tbx6 and Mesp2, and ultimately to understand how analog inputs (such as sequential wave patterns of oscillation) are converted into digital outputs (such as the square-like stair patterns of the segmental border).

Functions of Lfng in the posterior and anterior PSM during mouse somitogenesis

We also demonstrate from our present data that the oscillatory expression of *Lfng* is both required and sufficient for normal somitogenesis. However, this result will probably be viewed somewhat controversially given the recent findings that have underscored the significance of Lfng expression in the anterior PSM during this process, at least after E10.5 (Shifley et al., 2008; Stauber et al., 2009). The authors of these reports produced transgenic mice harboring *Lfng* expression without oscillation. Their data indicate that cNICD oscillation is disrupted, but that normal segmented somites form, after E10.5 and they concluded that oscillating *Lfng* expression is required only for early stage, but not later stage, somitogenesis (Shifley et al., 2008; Stauber et al., 2009). We wish therefore to discuss some possible explanations for the discrepancies between our current findings and these previous experimental results.

One possibility is that the common expression profiles between our *Hes7>Lfng* mouse and the mice studied in previous reports is important. We demonstrate here that *Hes7* and *Lfng* expression manifest a waved pattern within the Tbx6 expression domain, which includes a part of the anterior PSM. Therefore, in our *Hes7>Lfng* mouse, oscillating *Lfng* expression also exists in the anterior PSM, but not as a stabilized pattern. We suspect that the transgenic mice analyzed in previous reports lack oscillating *Lfng* expression in the posterior PSM but the oscillation might exist in the anterior PSM as well, and thus we speculate that the oscillating *Lfng* expression in the posterior PSM is not required after E10.5, but that in the anterior PSM might be sufficient for normal somitogenesis. Another possibility is that the slightly oscillating expression reported previously might be responsible for the rescue event. Previous studies have shown that two distinct enhancers are involved in the oscillatory expression of *Lfng*, one of which is disrupted in the mouse reported by Shifley et al. (Shifley et al., 2008), and a slight cyclic expression of *Lfng* exists in the mouse generated by Stauber et al. (Stauber et al., 2009). Hence, one possible interpretation for these discrepancies is that the slight cyclic expression of *Lfng* might be sufficient for normal development in the enhancer-specific

knockout mouse after E10.5 somitogenesis, but not prior to E10.5. It is reasonable to assume that the requirement of Notch clock oscillation by *Lfng* changes during somitogenesis and is lesser at later stages, as now suggested by a number of studies (Shifley et al., 2008; Stauber et al., 2009).

Acknowledgements
We thank Ryoichiro Kageyama (Kyoto University) for providing the *Hes7* promoter and enhancer cassette, Aya Satoh, Nobuo Sasaki and Yusuke Okubo (National Institute of Genetics) for animal care and the preparation of embryo samples and Mariko Ikumi, Eriko Ikeno and Shinobu Watanabe (National Institute of Health Sciences) for technical assistance. This work was supported in part by Grants-in-Aid for Scientific Research on Priority Areas, Dynamics of Extracellular Environments, and by the National BioResource Project from the Ministry of Education, Culture, Sports, Science and Technology, Japan.

Competing interests statement
The authors declare no competing financial interests.

Supplementary material
Supplementary material for this article is available at
http://dev.biologists.org/lookup/suppl/doi:10.1242/dev.044545/-/DC1

References
Aulehla, A. and Johnson, R. L. (1999). Dynamic expression of lunatic fringe suggests a link between notch signaling and an autonomous cellular oscillator driving somite segmentation. *Dev. Biol.* **207**, 49-61.
Aulehla, A., Wehrle, C., Brand-Saberi, B., Kemler, R., Gossler, A., Kanzler, B. and Herrmann, B. G. (2003). Wnt3a plays a major role in the segmentation clock controlling somitogenesis. *Dev. Cell* **4**, 395-406.
Aulehla, A., Wiegraebe, W., Baubet, V., Wahl, M. B., Deng, C., Taketo, M., Lewandoski, M. and Pourquie, O. (2008). A beta-catenin gradient links the clock and wavefront systems in mouse embryo segmentation. *Nat. Cell Biol.* **10**, 186-193.
Barrantes, I. B., Elia, A. J., Wunsch, K., Hrabe de Angelis, M. H., Mak, T. W., Rossant, J., Conlon, R. A., Gossler, A. and de la Pompa, J. L. (1999). Interaction between Notch signalling and Lunatic fringe during somite boundary formation in the mouse. *Curr. Biol.* **9**, 470-480.
Bessho, Y., Hirata, H., Masamizu, Y. and Kageyama, R. (2003). Periodic repression by the bHLH factor Hes7 is an essential mechanism for the somite segmentation clock. *Genes Dev.* **17**, 1451-1456.
Cole, S. E., Levorse, J. M., Tilghman, S. M. and Vogt, T. F. (2002). Clock regulatory elements control cyclic expression of Lunatic fringe during somitogenesis. *Dev. Cell* **3**, 75-84.
Dale, K. J. and Pourquie, O. (2000). A clock-work somite. *BioEssays* **22**, 72-83.
Delfini, M. C., Dubrulle, J., Malapert, P., Chal, J. and Pourquie, O. (2005). Control of the segmentation process by graded MAPK/ERK activation in the chick embryo. *Proc. Natl. Acad. Sci. USA* **102**, 11343-11348.
Dequeant, M. L. and Pourquie, O. (2008). Segmental patterning of the vertebrate embryonic axis. *Nat. Rev. Genet.* **9**, 370-382.
Dequeant, M. L., Glynn, E., Gaudenz, K., Wahl, M., Chen, J., Mushegian, A. and Pourquie, O. (2006). A complex oscillating network of signaling genes underlies the mouse segmentation clock. *Science* **314**, 1595-1598.
Evrard, Y. A., Lun, Y., Aulehla, A., Gan, L. and Johnson, R. L. (1998). lunatic fringe is an essential mediator of somite segmentation and patterning. *Nature* **394**, 377-381.
Feller, J., Schneider, A., Schuster-Gossler, K. and Gossler, A. (2008). Noncyclic Notch activity in the presomitic mesoderm demonstrates uncoupling of somite compartmentalization and boundary formation. *Genes Dev.* **22**, 2166-2171.
Horikawa, K., Ishimatsu, K., Yoshimoto, E., Kondo, S. and Takeda, H. (2006). Noise-resistant and synchronized oscillation of the segmentation clock. *Nature* **441**, 719-723.
Lewis, J. (2003). Autoinhibition with transcriptional delay: a simple mechanism for the zebrafish somitogenesis oscillator. *Curr. Biol.* **13**, 1398-1408.
McGrew, M. J., Dale, J. K., Fraboulet, S. and Pourquie, O. (1998). The lunatic fringe gene is a target of the molecular clock linked to somite segmentation in avian embryos. *Curr. Biol.* **8**, 979-982.
Morales, A. V., Yasuda, Y. and Ish-Horowicz, D. (2002). Periodic Lunatic fringe expression is controlled during segmentation by a cyclic transcriptional enhancer responsive to notch signaling. *Dev. Cell* **3**, 63-74.
Morimoto, M., Takahashi, Y., Endo, M. and Saga, Y. (2005). The Mesp2 transcription factor establishes segmental borders by suppressing Notch activity. *Nature* **435**, 354-359.
Nakajima, Y., Morimoto, M., Takahashi, Y., Koseki, H. and Saga, Y. (2006). Identification of Epha4 enhancer required for segmental expression and the regulation by Mesp2. *Development* **133**, 2517-2525.
Niwa, Y., Masamizu, Y., Liu, T., Nakayama, R., Deng, C. X. and Kageyama, R. (2007). The initiation and propagation of Hes7 oscillation are cooperatively regulated by Fgf and notch signaling in the somite segmentation clock. *Dev. Cell* **13**, 298-304.
Oginuma, M., Niwa, Y., Chapman, D. L. and Saga, Y. (2008). Mesp2 and Tbx6 cooperatively create periodic patterns coupled with the clock machinery during mouse somitogenesis. *Development* **135**, 2555-2562.
Ozbudak, E. M. and Lewis, J. (2008). Notch signalling synchronizes the zebrafish segmentation clock but is not needed to create somite boundaries. *PLoS Genet.* **4**, e15.
Palmeirim, I., Henrique, D., Ish-Horowicz, D. and Pourquie, O. (1997). Avian hairy gene expression identifies a molecular clock linked to vertebrate segmentation and somitogenesis. *Cell* **91**, 639-648.
Riedel-Kruse, I. H., Muller, C. and Oates, A. C. (2007). Synchrony dynamics during initiation, failure, and rescue of the segmentation clock. *Science* **317**, 1911-1915.
Sakai, K. and Miyazaki, J. (1997). A transgenic mouse line that retains Cre recombinase activity in mature oocytes irrespective of the cre transgene transmission. *Biochem. Biophys. Res. Commun.* **237**, 318-324.
Shifley, E. T., Vanhorn, K. M., Perez-Balaguer, A., Franklin, J. D., Weinstein, M. and Cole, S. E. (2008). Oscillatory lunatic fringe activity is crucial for segmentation of the anterior but not posterior skeleton. *Development* **135**, 899-908.
Stauber, M., Sachidanandan, C., Morgenstern, C. and Ish-Horowicz, D. (2009). Differential axial requirements for lunatic fringe and Hes7 transcription during mouse somitogenesis. *PLoS One* **4**, e7996.
Takahashi, Y., Koizumi, K., Takagi, A., Kitajima, S., Inoue, T., Koseki, H. and Saga, Y. (2000). Mesp2 initiates somite segmentation through the Notch signalling pathway. *Nat. Genet.* **25**, 390-396.
Takahashi, Y., Inoue, T., Gossler, A. and Saga, Y. (2003). Feedback loops comprising Dll1, Dll3 and Mesp2, and differential involvement of Psen1 are essential for rostrocaudal patterning of somites. *Development* **130**, 4259-4268.
Takahashi, Y., Yasuhiko, Y., Kitajima, S., Kanno, J. and Saga, Y. (2007). Appropriate suppression of Notch signaling by Mesp factors is essential for stripe pattern formation leading to segment boundary formation. *Dev. Biol.* **304**, 593-603.
Wahl, M. B., Deng, C., Lewandoski, M. and Pourquie, O. (2007). FGF signaling acts upstream of the NOTCH and WNT signaling pathways to control segmentation clock oscillations in mouse somitogenesis. *Development* **134**, 4033-4041.
Watanabe, T., Sato, Y., Saito, D., Tadokoro, R. and Takahashi, Y. (2009). EphrinB2 coordinates the formation of a morphological boundary and cell epithelialization during somite segmentation. *Proc. Natl. Acad. Sci. USA* **106**, 7467-7472.
Yasuhiko, Y., Haraguchi, S., Kitajima, S., Takahashi, Y., Kanno, J. and Saga, Y. (2006). Tbx6-mediated Notch signaling controls somite-specific Mesp2 expression. *Proc. Natl. Acad. Sci. USA* **103**, 3651-3656.
Zhang, N. and Gridley, T. (1998). Defects in somite formation in lunatic fringe-deficient mice. *Nature* **394**, 374-377.

FULL PAPER *Pathology*

Gene Expression Profiling and Cellular Distribution of Molecules with Altered Expression in the Hippocampal CA1 Region after Developmental Exposure to Anti-Thyroid Agents in Rats

Yukie SAEGUSA[1,2], Gye-Hyeong WOO[3], Hitoshi FUJIMOTO[3], Kaoru INOUE[3], Miwa TAKAHASHI[3], Masao HIROSE[3,4], Katsuhide IGARASHI[5], Jun KANNO[5], Kunitoshi MITSUMORI[1], Akiyoshi NISHIKAWA[3] and Makoto SHIBUTANI[1]*

[1]*Laboratory of Veterinary Pathology, Tokyo University of Agriculture and Technology, 3–5–8 Saiwai-cho, Fuchu-shi, Tokyo 183–8509,* [2]*Pathogenetic Veterinary Science, United Graduate School of Veterinary Sciences, Gifu University, 1–1 Yanagido, Gifu-shi, Gifu 501–1193,* [3]*Division of Pathology and* [5]*Division of Molecular Toxicology, National Institute of Health Sciences, 1–18–1 Kamiyoga, Setagaya-ku, Tokyo 158–8501 and* [4]*Food Safety Commission, Akasaka Park Bld. 22nd F., 5–2–20 Akasaka, Minato-ku, Tokyo 100–8989, Japan*

(Received 6 September 2009/Accepted 8 Octoberr 2009/Published online in J-STAGE 27 November 2009)

ABSTRACT. To determine whether developmental hypothyroidism causes permanent disruption of neuronal development, we first performed a global gene expression profiling study targeting hippocampal CA1 neurons in male rats at the end of maternal exposure to anti-thyroid agents on weaning (postnatal day 20). As a result, genes associated with nervous system development, zinc ion binding, apoptosis and cell adhesion were commonly up- or down-regulated. Genes related to calcium ion binding were up-regulated and those for myelination were often down-regulated. We, then, examined immunohistochemical cellular distribution of Ephrin type A receptor 5 (EphA5) and Tachykinin receptor (Tacr)-3, those selected based on the gene expression profiles, in the hippocampal formation at the adult stage (11-week-old) as well as at the end of exposure. At weaning, both EphA5- and Tacr3-immunoreactive cells with strong intensities appeared in the pyramidal cell layer or stratum oriens of the hippocampal CA1 region. Although the magnitude of the change was decreased at the adult stage, Tacr3 in the CA1 region showed a sustained increase in expressing cells until the adult stage after developmental hypothyroidism. On the other hand, EphA5-expressing cells did not show sustained increase at the adult stage. The results suggest that developmental hypothyroidism caused sustained neuronal expression of Tacr3 in the hippocampal CA1 region, probably reflecting a neuroprotective mechanism for mismigration.

KEY WORDS: developmental hypothyroidism, EphA5, hippocampal CA1 region, Tacr3.

J. Vet. Med. Sci. 72(2): 187–195, 2010

Thyroid hormones are essential for normal fetal and neonatal brain development. They control neuronal and glial proliferation in definitive brain regions and regulate neural migration and differentiation [12, 18, 21]. In humans, maternal hypothyroxinemia, early in pregnancy, may have adverse effects on fetal brain development and importantly, even mild-moderate hypothyroxinemia may result in suboptimal neurodevelopment [4]. These results may increase the concern of thyroid hormone-disrupting chemicals in the environment.

Experimentally, developmental hypothyroidism leads to growth retardation, neurological defects and impaired performance on a variety of behavioral learning actions [1, 2]. Rat offspring exposed maternally to anti-thyroid agents such as 6-propyl-2-thiouracil (PTU) show brain retardation, with impaired neuronal migration and white matter hypoplasia involving limited axonal myelination and oligodendrocytic accumulation [6, 8, 21]. The outcome of this type of brain retardation is permanent and is accompanied by apparent structural and functional abnormalities. However, it is still unclear whether the molecular aberrations remain in the retarded brain after maturation.

Histological lesion-specific gene expression profiling provides valuable information on the mechanisms underlying lesion development. We have established molecular analysis methods for DNA, RNA and proteins in paraffin-embedded small tissue specimens utilizing an organic solvent-based fixative, methacarn, with high performance close to that achieved with unfixed frozen tissue specimens [22, 26, 27]. We have previously applied these techniques to analyze global gene expression changes in microdissected lesions [23, 28].

Hippocampal CA1 region is a well-known target of developmental hypothyroidism [8], and we, in our recent study, detected a distribution variability of hippocampal CA1 pyramidal neurons reflecting mismigration in rat offspring at the adult stage after developmental exposure to anti-thyroid agents [24]. The present study was performed to determine whether developmental hypothyroidism triggers sustained aberrations in neuronal development associated with neuronal mismigration until the adult stage. For this purpose, we first performed a global gene expression profiling of the CA1-pyramidal cell layer in rat offspring at the end of developmental exposure to anti-thyroid agents. To distinguish chemical-specific expression changes from hypothyroidism-linked ones, two different anti-thyroid

* CORRESPONDENCE TO: SHIBUTANI, M., Laboratory of Veterinary Pathology, Tokyo University of Agriculture and Technology, 3–5–8 Saiwai-cho, Fuchu-shi, Tokyo 183–8509, Japan.
e-mail: mshibuta@cc.tuat.ac.jp

agents, PTU and 2-mercapto-1-methylimidazole (MMI), were used, and dose-related responses were also examined with PTU. To extract the neuronal cell layer-specific gene expression profile, microdissection technique was applied for microarray analysis. Based on the expression profiles obtained, cellular localization of the molecules showing altered expression were then immunohistochemically examined in the hippocampus at the adult stage as well as at the end of the developmental exposure.

MATERIALS AND METHODS

Chemicals and animals: 6-propyl-2-thiouracil (PTU; CAS No. 51–52–5) and methimazole (2-mercapto-1-methylimidazole: MMI; CAS No. 60–56–0) were obtained from Sigma Chemical Co. (St. Louis, MO, U.S.A.). Pregnant Crj:CD®(SD)IGS rats were purchased from Charles River Japan Inc. (Yokohama, Japan) at gestation day (GD) 3 (appearance of vaginal plugs was designated as GD 0). Animals were housed individually in polycarbonate cages with wood chip bedding, maintained in an air-conditioned animal room (temperature: 24 ± 1°C; relative humidity: 55 ± 5%) with a 12-hr light/dark cycle and allowed *ad libitum* access to food and tap water. A soy-free diet (Oriental Yeast Co., Ltd., Tokyo, Japan) was chosen as the basal diet for the maternal animals to eliminate possible phytoestrogen effects [10], and water was given *ad libitum* throughout the experimental period including the 1-week acclimation period.

Animal experiments: The animal experiments were identical to those in a previous study [24]. In brief, maternal animals were randomly divided into four groups including untreated controls. Eight dams per group were treated with 3 or 12 ppm of PTU or 200 ppm of MMI in the drinking water from GD 10 to postnatal day (PND) 20 (PND 0: the day of delivery). On PND 2, the litters were culled randomly, leaving four male and four female offspring. On PND 20, 20 male and 20 female offspring (at least one male and one female per dam) per group were subjected to prepubertal necropsy [13, 24].

The remaining animals were maintained until postnatal week (PNW) 11. All offspring consumed the CRF-1 basal diet and tap water *ad libitum* from PND 21 onwards. At PNW 11, all pups were subjected to adult stage necropsy [13, 24].

All animals used in the present study were weighed and sacrificed by exsanguination from the abdominal aorta under deep anesthesia. These protocols were reviewed in terms of animal welfare and approved by the Animal Care and Use Committee of the National Institute of Health Sciences, Japan.

Preparation of tissue specimens and microdissection: For microarray and subsequent real-time RT-PCR analyses, the whole brain of male offspring was removed at prepubertal necropsy on PND 20 (n=4/group) and was fixed with methacarn solution for 2 hr at 4°C [22]. Coronal brain slices taken at the position of –3.5 mm from the bregma were dehydrated and embedded in paraffin. The embedded tissue blocks were stored at 4°C until tissue sectioning for microdissection [9].

For microdissection, 4-μm-thick sections between ten 20 μm-thick serial sections were prepared. The 4 μm-thick sections were stained with hematoxylin and eosin for confirmation of anatomical orientation of the hippocampal substructure to aid microdissection. The 20 μm-thick sections were mounted onto PEN-foil film (Leica Microsystems GmbH, Welzlar, Germany) overlaid on glass slides, dried in an incubator overnight at 37°C, and then stained using an LCM staining kit (Ambion, Inc., Austin, TX, U.S.A.). Bilateral sides of the hippocampal CA1 pyramidal cell layer in the sections were subjected to laser microbeam microdissection (Leica Microsystems GmbH) (Fig. 1). Twenty sections from each animal were used for microdissection, and the bilateral microdissected samples were collected and stored in separate 1.5-m*l* sample tubes at –80°C until the extraction of total RNA.

RNA preparation, amplification and microarray analysis: Total RNA extraction from hippocampal CA1 samples, quantitation of the RNA yield, and amplification of RNA samples were performed using previously described methods [9, 28].

For microarray analysis, second-round-amplified biotin-labeled antisense RNAs were subjected to hybridization with a GeneChip® Rat Genome 230 2.0 Array (Affymetrix, Inc., Santa Clara, CA, U.S.A.), as previously described [28].

The selection of genes and normalization of the expression data were performed using GeneSpring® software (ver7.2, Silicon Genetics, Redwood City, CA, U.S.A.). Per chip normalization was performed according to a previously described method [28]. Genes showing signals judged to be "absent" in all eight samples of untreated controls and in the anti-thyroid agent-exposed group were excluded. Genes

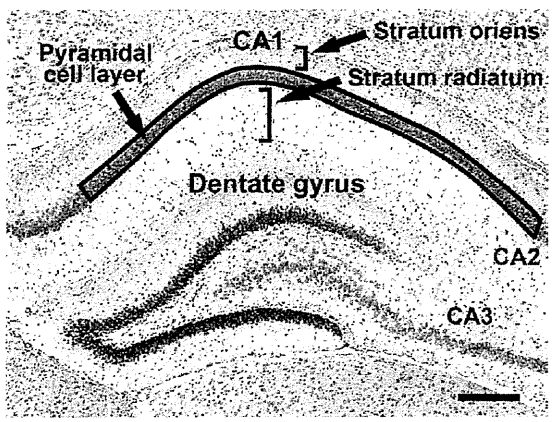

Fig. 1. Overview of the hippocampal formation of a male rat at postnatal day 20 stained with hematoxylin and eosin. Bar=200 μm. The CA1 pyramidal cell layer, enclosed by a solid line, was microdissected for the microarray and subsequent real-time RT-PCR analyses. The number of cells immunoreactive for the candidate molecules in this area was normalized for the length of CA1 used.

showing expression changes with differences of at least twofold in magnitude from the untreated controls were selected, and the "presence" signal in more than 3/4 of samples in each group showing higher expression values were selected. Genes showing altered expression in common in the anti-thyroid agent-exposed groups were also selected.

Real-time RT-PCR: Quantitative real-time RT-PCR was performed to confirm the expression values obtained with microarrays using an ABI Prism 7000 Sequence Detection System (Applied Biosystems Japan, Tokyo, Japan). Genes those showing altered expression (≥2-fold, ≤0.5-fold) in common in the anti-thyroid agent-exposed groups as compared with untreated control offspring were randomly selected, irrespective of the presence or absence of statistically significant difference. As a result, the following seven genes (four up-regulated and three down-regulated) with known function were selected as targets: Tachykinin receptor 3 (*Tacr3*), Calbindin 1, Slit homolog 2 (Drosophila) and Pleomorphic adenoma gene-like 1 (*Plagl1*) as up-regulated examples, and Myelin-associated oligodendrocytic basic protein (*Mobp*), Endothelial differentiation, sphingolipid G-protein-coupled receptor, 8 and CCAAT/enhancer binding protein as down-regulated. RT was performed using first-round antisense RNAs prepared for microarray analysis. For real-time PCR analysis of the genes selected, ABI Assays-on-Demand™ TaqMan® probe and primer sets from Applied Biosystems (available at https://products.appliedbiosystems.com/ab/en/US/adirect/ab?cmd=catNavigate2&catID=601267)(n=4/group) were used. For quantification of the expression data, a standard curve method was applied. The expression values were normalized to two housekeeping genes, Glyceraldehyde 3-phosphate dehydrogenase and Hypoxanthine-guanine phosphoribosyltransferase.

Immunohistochemistry: To evaluate the immunohistochemical distribution of the molecules selected by microarray analysis, the brains of male pups obtained at PND 20 or PNW 11 were fixed in Bouin's solution at room temperature overnight. Six animals were used as untreated controls, six for 200 ppm MMI, eight for 3 ppm PTU, and nine for 12 ppm PTU on PND 20. On PNW 11, 10 animals were used as untreated controls and 10 for 200 ppm MMI, nine for 3 ppm PTU, and six for 12 ppm PTU.

Immunohistochemistry was performed on the brain tissue sections of PND 20 and PNW 11 animals with antibodies against Ephrin type A receptor 5 (EphA5; rabbit IgG, 1:50; Abcam, Cambridge, U.K.) and Tacr3 (rabbit polyclonal antibody, 1:3,000, Novus Biologicals, Inc., Littleton, CO, U.S.A.), which were incubated with the tissue sections overnight at 4°C. Antigen retrieval treatment was not performed for these antigens. Immunodetection was carried out using a VECTASTAIN® Elite ABC kit (Vector Laboratories Inc., Burlingame, CA, U.S.A.) with 3,3'-diaminobenzidine/H_2O_2 as the chromogen, as previously described [23]. The sections were then counterstained with hematoxylin and coverslipped for microscopic examination.

With regard to EphA5, *Efna5*, a gene encoding the representative ligand for this receptor molecule [5], was found to be up-regulated (≥2-fold) by microarray analysis in all of the groups exposed to anti-thyroid agents in the present study (Table 1). Because distribution of EphA5 has been confirmed in the pyramidal cells of the hippocampal CA1 region at both developmental and adult stages in mice and at adult stage in humans [3, 17], we selected this molecule to examine distribution changes in the present study. Tacr3 was also up-regulated in all of the MMI and PTU groups by microarray analysis and real-time RT-PCR in the present study (Table 1). Expression of Tacr3 in the hippocampal CA1 pyramidal neurons has also been confirmed in rats [11], and therefore, we also selected this molecule for examination in the expression changes in the present study.

Morphometry of immunolocalized cells and apoptotic cells: EphA5- or Tacr3-immunoreactive cells distributed in the pyramidal cell layer or stratum oriens of the hippocampal CA1 region were bilaterally counted and normalized to the number in the length of the CA1 region measured (Fig. 1). Tacr3-immunoreactive cells in the subgranular zone of the dentate gyrus were also bilaterally counted and normalized for the number in the length of the granular zone measured. For quantitative measurement of each immunoreactive cellular component, digital photomicrographs at 100-fold magnification were taken using a BX51 microscope (Olympus Optical Co., Ltd., Tokyo, Japan) attached to a DP70 Digital Camera System (Olympus Optical Co., Ltd.), and quantitative measurements were performed using the WinROOF image analysis software package (version 5.7, Mitani Corp., Fukui, Japan).

Statistical analysis: Numerical data of the number of immunoreactive cells were assessed using Student's *t*-test to compare the untreated controls with each of the anti-thyroid agent-exposed groups when the variance was homogenous among the groups using a test for equal variance. If a significant difference in variance was observed, Aspin-Welch's *t*-test was used instead. The data for gene expression levels from real-time RT-PCR analysis were analyzed by the Kruskal-Wallis test, followed by Bartlett's test. When statistically significant differences were indicated, Dunnett's multiple test was used for comparisons with the untreated controls. For the microarray data, statistical analysis was performed with GeneSpring® software, and the significance of gene expression changes was analyzed by Student's *t*-test or ANOVA between the untreated controls and each of the anti-thyroid agent-exposed groups.

RESULTS

Microarray analysis: Figure 2 shows the Venn diagram of genes showing altered expression in the microdissected CA1 pyramidal neurons in the exposure groups in combination or individually in each exposure group. Many genes were found to be up- or down-regulated in common in two of the three groups. The numbers of genes classified into common categories between the groups or individually in each group were similar in terms of up- and down-regulated genes. The number of genes showing up- or down-regula-

Table 1. List of representative genes showing up- or down-regulation common to 2-mercapto-1-methylimidazole (MMI), 3 and 12 ppm 6-propyl-2-thiouracil (PTU) (≥2-fold, ≤0.5-fold)

Gene function	Accession No.	Gene title	Symbol	MMI	3 ppm PTU	12 ppm PTU
Up-regulated genes (of 119 genes in total)						
Nervous system development	AI101660	Slit homolog 2 (Drosophila)	Slit2	3.04	2.62	7.08
Nervous system development	NM_024358.1	Notch gene homolog 2 (Drosophila)	Notch2	2.52	2.01	2.02
Nervous system development	AW527295	Ephrin A5	Efna5	3.12	3.46	4.31
Nervous system development	NM_053465.1	Fucosyltransferase 9	Fut9	2.13	6.75	2.11
Nervous system development	BE106256	Sparc/osteonectin, cwcv and kazal-like domains proteoglycan 1	Spock1	3.22	3.13	2.15
Calcium ion binding	X04280.1	Calbindin 1	Calb1	4.48	4.85	9.00
Calcium ion binding	BM386119	UDP-N-acetyl-alpha-D-galactosamine:polypeptide N-acetylgalactosaminyltransferase 3 (GalNAc-T3)	Galnt3	2.43	2.30	2.63
Calcium ion binding	BI279663	Desmocollin 2	Dsc2	2.82	2.04	5.62
Calcium ion binding	AI105369	Calmodulin-like 4	Calml4	3.40	2.25	5.59
Zinc ion binding	BE098686	Similar to Tnf receptor-associated factor 1	LOC687813	3.10	2.04	2.78
Zinc ion binding	BF562032	RAN binding protein 2	Ranbp2	3.49	2.67	2.78
Zinc ion binding	BF397925	ADAMTS-like 1	Adamtsl1	6.22	2.55	7.63
Zinc ion binding	BF395606	Splicing factor, arginine/serine-rich 7	Sfrs7	4.93	2.06	2.90
Apoptosis	NM_012760.1	Pleomorphic adenoma gene-like 1	Plagl1	3.10	4.28	6.86
Apoptosis	NM_057130.1	Harakiri, BCL2 interacting protein (contains only BH3 domain)	Hrk	2.63	2.73	3.18
Cell Adhesion	AA850909	Poliovirus receptor-related 2	Pvrl2	4.74	2.46	2.61
Cell Adhesion	AA819731	Hyaluronan and proteoglycan link protein 4	Hapln4	4.13	6.67	3.46
Cell Adhesion	BI287851	Collagen, type VI, alpha 2	Col6a2	3.45	2.19	5.12
Ion channel activity	AA851939	FXYD domain-containing ion transport regulator 6	Fxyd6	4.73	2.61	7.85
Other	NM_017053.1	Tachykinin receptor 3	Tacr3	7.32	6.19	12.49
Down-regulated genes (of 97 genes in total)						
Nervous system development	NM_031018.1	Activating transcription factor 2	Atf2	0.41	0.36	0.36
Neuron migration	BF390065	Roundabout homolog 3 (Drosophila)	Robo3	0.06	0.31	0.04
Neuron differentiation	AF115249.1	Endothelial differentiation, sphingolipid G-protein-coupled receptor, 8	Edg8	0.40	0.06	0.08
Neuron differentiation	NM_024125.1	CCAAT/enhancer binding protein (C/EBP), beta	Cebpb	0.31	0.43	0.26
Myelination	X89638.1	Myelin-associated oligodendrocytic basic protein	Mobp	0.35	0.18	0.12
Myelination	NM_017190.1	Myelin-associated glycoprotein	Mag	0.47	0.36	0.29
Myelination	NM_022668.1	Myelin oligodendrocyte glycoprotein	Mog	0.44	0.32	0.19
Myelination	NM_012798.1	Mal, T-cell differentiation protein	Mal	0.37	0.28	0.28
Myelination	AA945178	Signal recognition particle receptor, B subunit transferrin	Srprb Tf	0.33	0.27	0.15
Zinc ion binding	NM_012566.1	Growth factor independent 1 transcription repressor	Gfi1	0.20	0.44	0.41
Zinc ion binding	AW529624	Zinc finger protein 91	Zfp91	0.33	0.32	0.38
Actin binding	AW522439	Ermin, ERM-like protein	Ermn	0.43	0.42	0.28
Apoptosis	BG377720	Solute carrier family 5 (sodium/glucose cotransporter), member 11	Slc5a11	0.25	0.19	0.19
Apoptosis	U21955.1	Eph receptor A	Epha7	0.34	0.48	0.18
Cell Adhesion	BM391100	Mucin 4, cell surface associated	Muc4	0.43	0.36	0.27
Other	AW435010	Protein tyrosine phosphatase, non-receptor type 3	Ptpn3	0.38	0.46	0.36
Other	AF312319.1	gamma-aminobutyric acid (GABA) B receptor 1	Gabbr1	0.33	0.41	0.39
Other	NM_053936.1	Endothelial differentiation, lysophosphatidic acid G-protein-coupled receptor, 2	Edg2	0.47	0.31	0.31

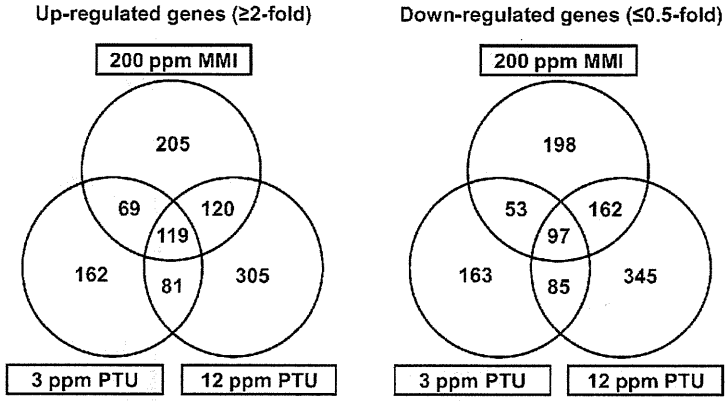

Fig. 2. Venn diagram of gene populations showing altered expression in the hippocampal CA1 pyramidal cell layer at postnatal day 20 in response to maternal exposure to propylthiouracil and/or 2-mercapto-1-methylimidazole compared with the untreated controls. (Left) Up-regulated genes (≥2-fold). (Right) Down-regulated genes (≤0.5-fold). Abbreviations: MMI, 2-mercapto-1-methylimidazole; PTU, 6-propyl-2-thiouracil.

Table 2. Validation of microarray data by real-time RT-PCR

Gene	200 ppm MMI			3 ppm PTU			12 ppm PTU		
	Microarray	Real-time RT-PCR normalized to		Microarray	Real-time RT-PCR normalized to		Microarray	Real-time RT-PCR normalized to	
		Hprt[a)]	Gapdh[b)]		Hprt	Gapdh		Hprt	Gapdh
Tacr3[c)]	7.32 ± 2.21**	4.29 ± 1.27	4.08 ± 1.15*	6.19 ± 2.19**	3.46 ± 1.42	3.76 ± 1.51*	12.49 ± 1.56**	9.23 ± 3.00**	8.81 ± 1.60**
Calb1[d)]	4.48 ± 0.66*	3.96 ± 0.74	3.67 ± 0.16	4.85 ± 2.53*	4.74 ± 2.48	4.93 ± 3.79	9.00 ± 1.85**	11.13 ± 2.13**	10.53 ± 3.26**
Slit2[e)]	3.04 ± 0.79	2.83 ± 0.90	4.08 ± 1.15*	2.62 ± 1.16	1.33 ± 0.67	3.67 ± 1.51*	7.08 ± 2.15**	4.72 ± 2.57**	8.81 ± 1.60**
Plgl1[f)]	3.10 ± 1.57	12.67 ± 5.00	11.5 ± 7.50	4.28 ± 2.88	18.33 ± 6.00	19.00 ± 9.00*	6.86 ± 2.85**	30.67 ± 5.33**	27.00 ± 8.00**
Mobp[g)]	0.35 ± 0.15**	0.6 ± 0.22*	0.52 ± 0.16**	0.18 ± 0.07**	0.24 ± 0.07**	0.24 ± 0.05**	0.12 ± 0.02**	0.18 ± 0.04**	0.16 ± 0.04**
Edg8[h)]	0.40 ± 0.11*	0.49 ± 0.16*	0.43 ± 0.13*	0.06 ± 0.05**	0.29 ± 0.10**	0.28 ± 0.08**	0.08 ± 0.07**	0.21 ± 0.07**	0.18 ± 0.03**
Cebpb[i)]	0.31 ± 0.06**	0.43 ± 0.04**	0.38 ± 0.06**	0.43 ± 0.18**	0.77 ± 0.07	0.76 ± 0.10	0.26 ± 0.04**	0.39 ± 0.16**	0.35 ± 0.22**

a) Hprt, Hypoxanthine-guanine phosphoribosyltransferase; b) Gapdh, Glyceraldehyde 3-phosphate dehydrogenase; c) Tacr3, Tachykinin receptor 3; d) Calb1, Calbindin 1; e) Slit2, Slit homolog 2 (Drosophila); f) Plgl1, Pleomorphic adenoma gene-like 1; g) Mobp, Myelin-associated oligodendrocytic basic protein; h) Edg8, Endothelial differentiation, sphingolipid G-protein-coupled receptor, 8; i) Cebpb, CCAAT/enhancer binding protein (C/EBP), beta.

Values are mean ± SD (n=4) relative to the expression level in the untreated controls. Real-time RT-PCR analysis of Hprt and Gapdh was performed in the analysis of each target gene.

*, **: Significantly different from the untreated controls at $P<0.05$ and $P<0.01$, respectively (Dunnett's multiple comparison test).

tion in response to 12 ppm PTU was approximately 2-fold higher than that with 3 ppm PTU. The number of genes showing up- or down-regulation in response to 200 ppm MMI was in between that elicited by 3 or 12 ppm PTU. One-hundred nineteen genes were up-regulated in common by MMI and PTU, with PTU showing up-regulation from 3 ppm. On the other hand, 97 genes showed down-regulation in all MMI and PTU groups. Representative genes showing up- or down-regulation in all three groups are shown in the Table 1. Among the genes listed, genes associated with nervous system development, zinc ion binding, apoptosis and cell adhesion were commonly up- or down-regulated. Genes related to calcium ion binding were found to be up-regulated and those for myelination were often down-regulated.

Real-time RT-PCR analysis: For confirmation of the microarray data, four genes that were up-regulated and three that were down-regulated in response to anti-thyroid agents were selected for mRNA expression analysis by real-time RT-PCR and the results are summarized in Table 2.

In all exposure groups, many of the expression changes were similar in the two analysis systems, except for much higher expression of *Plagl1* in all exposure groups by real-time RT-PCR as compared with findings from the microarray system.

Although we performed expression analysis of *Efna5* by real-time RT-PCR, expression values were rather low with great variability between samples, and therefore, reliable quantitative data could not be obtained (data not shown).

Immunolocalization of EphA5 and Tacr3 in the hippoc-

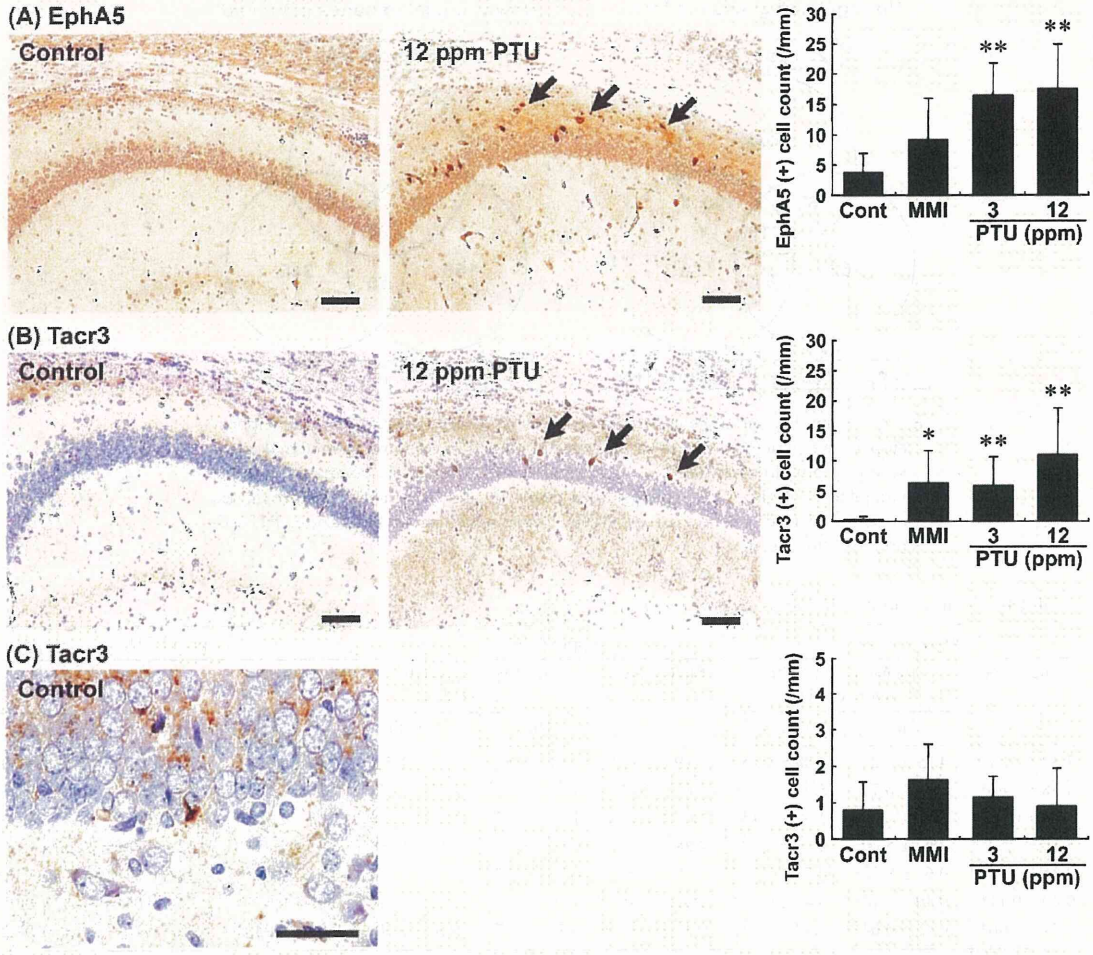

Fig. 3. Distribution of immunoreactive cells for EphA5 and Tacr3 in the hippocampal formation in rats at PND 20 after maternal exposure to anti-thyroid agents. (A) EphA5-immunoreactive cells with strong intensity located within the pyramidal cell layer and stratum oriens of the hippocampal CA1 region (arrows). Note the higher number of EphA5-positive cells in a case exposed to 12 ppm PTU (Right) as compared with the control animal (Left). Bar =100 μm. The graph shows the number of EphA5-positive cells/unit length (mm) of the CA1 region of the bilateral hemispheres. ** $P<0.01$ versus untreated controls (Student's *t*-test). (B) Tacr3-immunoreactive cells with strong intensity located within the pyramidal cell layer and stratum oriens of the hippocampal CA1 region (arrows). Note the higher number of Tacr3-positive cells in a case exposed to 12 ppm PTU (Right) as compared with the control animal (Left). Bar =100 μm. The graph shows the number of Tacr3-positive cells/unit length (mm) of the CA1 region of bilateral hemispheres. * $P<0.05$, ** $P<0.01$ versus untreated controls (Student's *t*-test). (C) Tacr3-immunoreactive cells located in the subgranular zone of the dentate gyrus. Bar =50 μm. The graph shows the number of Tacr3-positive cells/unit length (mm) of the subgranular zone of bilateral hemispheres. Abbreviations: EphA5, Ephrin type A receptor 5; MMI, 2-mercapto-1-methylimidazole; PTU, 6-propyl-2-thiouracil, Tacr3, Tachykinin receptor 3.

ampal formation: Immunohistochemical localization of EphA5 and Tacr3 in the hippocampal formation was examined at PND 20 and PNW 11.

On PND 20, EphA5 showed weak immunoreactivity in the pyramidal neurons throughout the hippocampal formation in the untreated controls. This immunoreactivity was unchanged by exposure to anti-thyroid agents. On the other hand, very sparse distribution of strongly immunoreactive cells for EphA5 was observed in the region of the CA1 pyramidal cell layer and stratum oriens in the untreated control animals, but immunoreactive cells were significantly increased showing scattered distribution by PTU at both 3 and 12 ppm (Fig. 3A). MMI-exposed animals also showed a small increase in the number of strongly positive cells with EphA5. Increased intensity in immunoreactivity of EphA5 was also observed in the gray matter consisting of neuropil at the stratum oriens of the CA1 region (Fig. 3A), and also in the molecular layer of the dentate gyrus at PND 20 after exposure to anti-thyroid agents, especially in PTU-exposed groups (data not shown).

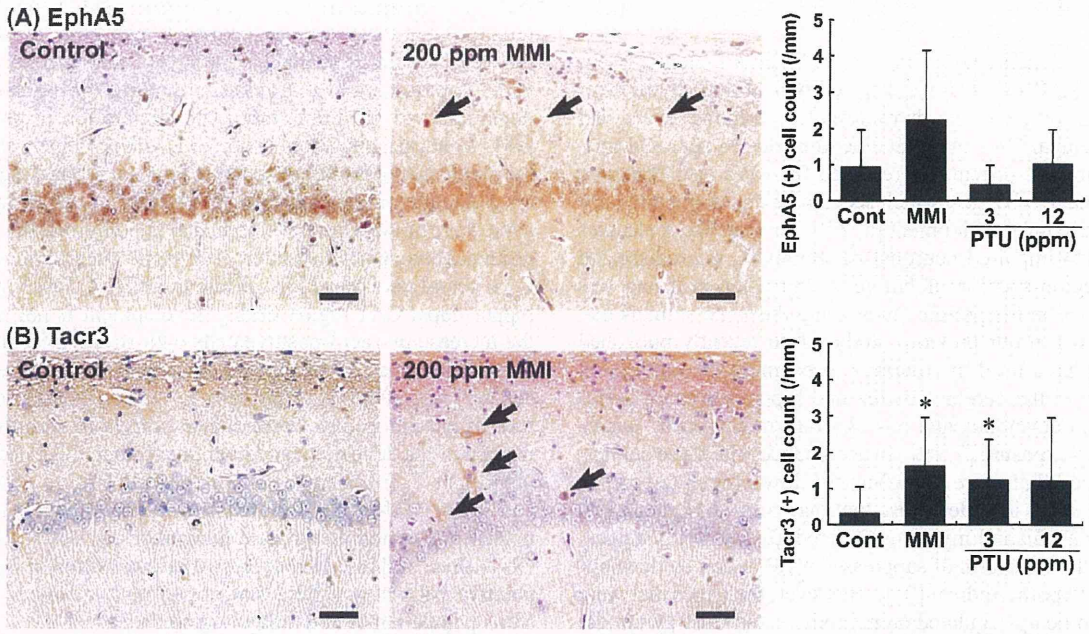

Fig. 4. Distribution of immunoreactive cells for EphA5 and Tacr3 in the hippocampal formation at PNW 11 of rats exposed maternally to anti-thyroid agents. (A) EphA5-immunoreactive cells with moderate staining intensity located within the pyramidal cell layer and stratum oriens of the hippocampal CA1 region. EphA5-positive cells in a case exposed to 200 ppm MMI (Right) as compared with the control animal (Left). The arrows show positive cells. Bar =50 μm. The graph shows the number of EphA5-positive cells/unit length (mm) of the CA1 region of the bilateral hemispheres. (B) Tacr3-immunoreactive cells with weak to moderate staining intensity located within the pyramidal cell layer and stratum oriens of the hippocampal CA1 region (arrows). Immunoreactivity is rather faint as compared with that observed at PND 20. Note the higher number of Tacr3-positive cells in a case exposed to 200 ppm MMI (Right) as compared with the control animal (Left). Bar =50 μm. The graph shows the number of Tacr3-positive cells/unit length (mm) of the CA1 region of bilateral hemispheres. * $P<0.05$ versus untreated controls (Student's t-test). Abbreviations: EphA5, Ephrin type A receptor 5; MMI, 2-mercapto-1-methylimidazole; PTU, 6-propyl-2-thiouracil; Tacr3, Tachykinin receptor 3.

With regards to Tacr3, the number of positive cells was increased with a scattered distribution showing strong intensity in the CA1 region similarly to that of EphA5 in the animals exposed to MMI or PTU on PND 20, but they were mostly absent in the untreated controls (Fig. 3B). Similarly, Tacr3-immunoreactive cells were sparse in the subgranular zone of the dentate gyrus in the MMI and PTU-exposed animals and in the untreated controls, but there were no differences in the number of positive cells as compared with the untreated controls (Fig. 3C). In addition, increased intensity in neuropil-immunoreactivity of Tacr3 was also observed in the strata oriens and radiatum of the CA1 region in all exposure groups of anti-thyroid agents (Fig. 3B).

On PNW 11, EphA5 showed weak immunoreactivity in the pyramidal neurons throughout the hippocampal formation in the untreated controls. This immunoreactivity was unchanged by exposure to anti-thyroid agents. EphA5-immunoreactive cells with moderate staining intensity were very sparsely observed in the region of the CA1 pyramidal cell layer and stratum oriens in the untreated control animals. There was no statistically significant increase in the number of these immunoreactive cells after exposure to PTU, while animals exposed to MMI showed a tendency for an increased number of immunoreactive cells (Fig. 4A). Increased neuropil-immunoreactivity of EphA5 as observed at PND 20 in exposure groups of anti-thyroid agents was mostly disappeared at PNW 11 (data not shown).

As well as at PND 20, Tacr3-immunoreactive cells were mostly absent in the untreated controls at PNW 11; however, a few immunoreactive cells with weak to moderate intensity were observed in the stratum oriens of the CA1 region in the animals exposed to anti-thyroid agents. There was a statistically significant difference in the animals treated with MMI or 3 ppm PTU compared with the untreated controls (Fig. 4B). Although the change was non-significant and lacked dose-dependence, 12 ppm PTU also showed an increasing tendency in the number of Tacr3-immunoreactive cells. In addition, increased neuropil-immunoreactivity of Tacr3 as observed at PND 20 in exposure groups of anti-thyroid agents was mostly disappeared at PNW 11 (data not shown).

DISCUSSION

In our recent study using rats [24], after maternal exposure to MMI or PTU, we detected typical hypothyroidism-related changes in the thyroid-related hormone levels, and hippocampal CA1 pyramidal neurons due to neuronal mismigration, as previously reported [8]. We also observed white matter changes, which seem to be due to impaired oligodendroglial development [6, 21]. To visualize molecules related to impaired neuronal development, microdissected CA1 region-specific global gene expression profiling was performed in the present study using the same animals that were used in our previous study. Two recently published studies have used microarrays to examine the expression profiles in the cerebral cortex and hippocampus of genes linked to developmental hypothyroidism caused by maternal PTU-exposure [7, 19]. In accordance with these studies, the genes that were significantly down-regulated in the present study included those that play roles in myelination, such as *Mobp* and myelin-associated glycoprotein, suggestive of the reflection of suppressed myelination by developmental hypothyroidism [21]. However, the genes that were found to be up-regulated on microdissected CA1 pyramidal cell layer, including *Efna5* and *Tacr3*, in the present study, have not been identified in previous studies. This difference may be related to the target tissues collected and the methods used, including microdissection of CA1 pyramidal cell layer from paraffin-embedded sections in the present study versus manual dissection of the cortical tissues from unfixed tissues in the previous studies.

EphA5 is a tyrosine kinase receptor that is almost exclusively expressed in the nervous system [15]. EphA5 and its ligand are important in mediating axon guidance, topographic projection, development, cell migration and the plasticity of limbic structures [15]. In addition, the transient expression of EphA5 during development is correlated with early neurogenesis and the migration of differentiated cells in the midbrain [3]. Thus, although expression of EphA5 was mostly weak in the euthyroid CA1 pyramidal neurons at PND 20, the increased number of EphA5-expressing cells with strong intensity in the CA1 region during developmental hypothyroidism in the present study reflects the neuronal mismigration caused by anti-thyroid agents. However, this increase was recovered after cessation of developmental hypothyroidism. Ephrins and their receptors are recently identified molecules and functional relationship between subfamily proteins is largely unknown; however, we, in the present study, found down-regulation of Epha7, another subfamily ephrin receptor, in all exposure groups of anti-thyroid agents (Table 1).

Tacr3, a member of the mammalian tachykinin peptide neurotransmitter/neuromodulator receptor family, is predominantly expressed in neurons in both the peripheral and central nervous systems, including the hippocampus [25]. There is increasing evidence of the role of Tacr3 on the survival and function of dopaminergic neurons. The survival of mesencephalic dopaminergic neurons during development largely depends on excitatory inputs, and tachykinins, through their receptors, are reported to play role in excitation [20]. On the other hand, senktide, a Tacr3 agonist, activates dopaminergic neurons to stimulate the release of dopamine and serotonin, and hyperlocomotion in gerbils [14]. Abnormal excitatory action of D_2-like receptor, one of the major subtypes of dopaminergic receptors, was observed on glutamatergic transmission in the CA1 synapses in the adult stage of rats after developmental hypothyroidism, suggesting a permanent disruption of synaptic integration in the CA1 neural networks [16]. While the role of Tacr3 in the hippocampal CA1 region during development is not clear, the increase in Tacr3-positive cells with strong intensity in this region during developmental hypothyroidism suggests a cell survival effect of tachykinin-3. Although the magnitude of the change was decreased, as compared with that at the end of the developmental hypothyroidism, the increased number of Tacr3-positive cells in the CA1 region of MMI and 3 ppm PTU-exposed animals may be an outcome of permanent disruption of synaptic integration, as described by Oh-Nishi *et al.* [16]. However, sparse distribution of Tacr3-positive cells may reflect that impairment sustained in a small population of aberrantly migrated neurons.

In conclusion, in this study, we have shown gene expression profiles showing altered expression in response to developmental hypothyroidism by analysis on microdissected hippocampal CA1 pyramidal cell layer in rats. Immunohistochemical analysis of the two candidate molecules revealed that developmental hypothyroidism until weaning is associated with the persistence of Tacr3-expressing neurons until the adult stage in the CA1 region, suggestive of the reflection of permanent disruption of synaptic integration. These findings probably reflect a mechanism to facilitate cell survival of aberrantly developed neurons due to mismigration.

ACKNOWLEDGMENT(S). We thank Miss Tomomi Morikawa for her technical assistance in conducting the animal study. We also thank Mrs. Shigeko Suzuki and Miss Ayako Kaneko for their technical assistance in preparing the histological specimens. This work was supported in part by Health and Labour Sciences Research Grants (Research on Risk of Chemical Substances) from the Ministry of Health, Labour and Welfare of Japan. All of the authors disclose that there are no conflicts of interest that could inappropriately influence the outcomes of the present study.

REFERENCES

1. Akaike, M., Kato, N., Ohno, H. and Kobayashi, T. 1991. Hyperactivity and spatial maze learning impairment of adult rats with temporary neonatal hypothyroidism. *Neurotoxicol. Teratol.* **13**: 317–322.
2. Comer, C. P. and Norton, S. 1982. Effects of perinatal methimazole exposure on a developmental test battery for neurobehavioral toxicity in rats. *Toxicol. Appl. Pharmacol.* **63**: 133–141.
3. Cooper, M. A., Crockett, D. P., Nowakowski, R. S., Gale, N. W. and Zhou, R. 2009. Distribution of EphA5 receptor protein

in the developing and adult mouse nervous system. *J. Comp. Neurol.* **514**: 310–328.
4. de Escobar, G. M., Obregón, M. J. and del Rey, F. E. 2007. Iodine deficiency and brain development in the first half of pregnancy. *Public Health Nutr.* **10**: 1554–1570.
5. Gerlai, R., Shinsky, N., Shih, A., Williams, P., Winer, J., Armanini, M., Cairns, B., Winslow, J., Gao, W. and Phillips, H. S. 1999. Regulation of learning by EphA receptors: a protein targeting study. *J. Neurosci.* **19**: 9538–9549.
6. Goodman, J. H. and Gilbert, M. E. 2007. Modest thyroid hormone insufficiency during development induces a cellular malformation in the corpus callosum: a model of cortical dysplasia. *Endocrinology* **148**: 2593–2597.
7. Kobayashi, K., Akune, H., Sumida, K., Saito, K., Yoshioka, T. and Tsuji, R. 2009. Perinatal exposure to PTU decreases expression of Arc, Homer 1, Egr 1 and Kcna 1 in the rat cerebral cortex and hippocampus. *Brain Res.* **1264**: 24–32.
8. Lavado-Autric, R., Ausó, E., García-Velasco, J. V., Arufe Mdel, C., Escobar del Rey, F., Berbel, P. and Morreale de Escobar, G. 2003. Early maternal hypothyroxinemia alters histogenesis and cerebral cortex cytoarchitecture of the progeny. *J. Clin. Invest.* **111**: 954–957.
9. Lee, K-Y., Shibutani, M., Inoue, K., Kuroiwa, K., U, M., Woo, G-H. and Hirose, M. 2006. Methacarn fixation—Effects of tissue processing and storage conditions on detection of mRNAs and proteins in paraffin-embedded tissues. *Anal. Biochem.* **351**: 36–43.
10. Masutomi, N., Shibutani, M., Takagi, H., Uneyama, C., Takahashi, N. and Hirose, M. 2003. Impact of dietary exposure to methoxychlor, genistein, or diisononyl phthalate during the perinatal period on the development of the rat endocrine/reproductive systems in later life. *Toxicology* **192**: 149–170.
11. Mileusnic, D., Lee, J. M., Magnuson, D. J., Hejna, M. J., Krause, J. E., Lorens, J. B. and Lorens, S. A. 1999. Neurokinin-3 receptor distribution in rat and human brain: an immunohistochemical study. *Neuroscience* **89**: 1269–1290.
12. Montero-Pedrazuela, A., Venero, C., Lavado-Autric, R., Fernández-Lamo, I., García-Verdugo, J. M., Bernal, J. and Guadaño-Ferraz, A. 2006. Modulation of adult hippocampal neurogenesis by thyroid hormones: implications in depressive-like behavior. *Mol. Psychiatry* **11**: 361–371.
13. Nakamura, R., Teshima, R., Hachisuka, A., Sato, Y., Takagi, K., Nakamura, R., Woo, G-H., Shibutani, M. and Sawada, J. 2007. Effects of developmental hypothyroidism induced by maternal administration of methimazole or propylthiouracil on the immune system of rats. *Int. Immunopharmacol.* **7**: 1630–1638.
14. Nordquist, R. E., Durkin, S., Jacquet, A. and Spooren, W. 2008. The tachykinin NK3 receptor agonist senktide induces locomotor activity in male Mongolian gerbils. *Eur. J. Pharmacol.* **600**: 87–92.
15. Numachi, Y., Yoshida, S., Yamashita, M., Fujiyama, K., Toda, S., Matsuoka, H., Kajii, Y. and Nishikawa, T. 2007. Altered EphA5 mRNA expression in rat brain with a single methamphetamine treatment. *Neurosci. Lett.* **424**: 116–121.
16 Oh-Nishi, A., Saji, M., Furudate, S. I. and Suzuki, N. 2005. Dopamine D_2-like receptor function is converted from excitatory to inhibitory by thyroxine in the developmental hippocampus. *J. Neuroendocrinol.* **17**: 836–845.
17. Olivieri, G. and Miescher, G. C. 1999. Immunohistochemical localization of EphA5 in the adult human central nervous system. *J. Histochem. Cytochem.* **47**: 855–861.
18. Porterfield, S. P. 2000. Thyroidal dysfunction and environmental chemicals—Potential impact on brain development. *Environ. Health Perspect.* **108**: 433–438.
19. Royland, J. E., Parker, J. S. and Gilbert, M. E. 2008. A genomic analysis of subclinical hypothyroidism in hippocampus and neocortex of the developing rat brain. *J. Neuroendocrinol.* **20**: 1319–1338.
20. Salthun-Lassalle, B., Traver, S., Hirsch, E. C. and Michel, P. P. 2005. Substance P, neurokinins A and B, and synthetic tachykinin peptides protect mesencephalic dopaminergic neurons in culture via an activity-dependent mechanism. *Mol. Pharmacol.* **68**: 1214–1224.
21. Schoonover, C. M., Seibel, M. M., Jolson, D. M., Stack, M. J., Rahman, R. J., Jones, S. A., Mariash, C. N. and Anderson, G. W. 2004 Thyroid hormone regulates oligodendrocyte accumulation in developing rat brain white matter tracts. *Endocrinology* **145**: 5013–5020.
22. Shibutani, M., Uneyama, C., Miyazaki, K., Toyoda, K. and Hirose, M. 2000. Methacarn fixation: a novel tool for analysis of gene expressions in paraffin-embedded tissue specimens. *Lab. Invest.* **80**: 199–208.
23. Shibutani, M., Lee, K-Y., Igarashi, K., Woo, G-H., Inoue, K., Nishimura, T. and Hirose, M. 2007. Hypothalamus region-specific global gene expression profiling in early stages of central endocrine disruption in rat neonates injected with estradiol benzoate or flutamide. *Dev. Neurobiol.* **67**: 253–269.
24. Shibutani, M., Woo, G-H., Fujimoto, H., Saegusa, Y., Takahashi, M., Inoue, K., Hirose, M. and Nishikawa, A. 2009. Assessment of developmental effects of hypothyroidism in rats from in utero and lactation exposure to anti-thyroid agents. *Reprod. Toxicol.* **28**: 297–307.
25. Smith, P. W. and Dawson, L. A. 2008. Neurokinin 3 (NK3) receptor modulators for the treatment of psychiatric disorders. *Recent Pat. CNS Drug Discov.* **3**: 1–15.
26. Takagi, H., Shibutani, M., Kato, N., Fujita, H., Lee, K-Y., Takigami, S., Mitsumori, K. and Hirose, M. 2004. Microdissected region-specific gene expression analysis with methacarn-fixed, paraffin-embedded tissues by real-time RT-PCR. *J. Histochem. Cytochem.* **52**: 903–913.
27. Uneyama, C., Shibutani, M., Masutomi, N., Takagi, H. and Hirose, M. 2002. Methacarn fixation for genomic DNA analysis in microdissected, paraffin-embedded tissue specimens. *J. Histochem. Cytochem.* **50**: 1237–1245.
28. Woo, G-H., Takahashi, M., Inoue, K., Fujimoto, H., Igarashi, K., Kanno, J., Hirose, M., Nishikawa, A. and Shibutani, M. 2009. Cellular distributions of molecules with altered expression specific to thyroid proliferative lesions developing in a rat thyroid carcinogenesis model. *Cancer Sci.* **100**: 617–625.

NANOS2 interacts with the CCR4-NOT deadenylation complex and leads to suppression of specific RNAs

Atsushi Suzuki[a], Katsuhide Igarashi[b], Ken-ichi Aisaki[b], Jun Kanno[b], and Yumiko Saga[c,1]

[a]Interdisciplinary Research Center, Yokohama National University, Yokohama, Kanagawa 240-8501, Japan; [b]Cellular and Molecular Toxicology Division, National Institute of Health Sciences, Setagayaku, Tokyo 158-8501, Japan; and [c]Division of Mammalian Development, National Institute of Genetics, Mishima 411-8540, Japan

Edited by Ruth Lehmann, New York University Medical Center, New York, NY, and approved December 30, 2009 (received for review August 2, 2009)

Nanos is one of the evolutionarily conserved proteins implicated in germ cell development. We have previously shown that NANOS2 plays an important role in both the maintenance and sexual development of germ cells. However, the molecular mechanisms underlying these events have remained elusive. In our present study, we found that NANOS2 localizes to the P-bodies, known centers of RNA degradation that are abundantly accumulated in male gonocytes. We further identified by immunoprecipitation that the components of the CCR4-NOT deadenylation complex are NANOS2-interacting proteins and found that NANOS2 promotes the localization of CNOT proteins to P-bodies in vivo. We also elucidated that the NANOS2/CCR4-NOT complex has deadenylase activity in vitro, and that some of the RNAs implicated in meiosis interact with NANOS2 and are accumulated in its absence. Our current data thus indicate that the expression of these RNA molecules is normally suppressed via a NANOS2-mediated mechanism. We propose from our current findings that NANOS2-interacting RNAs may be recruited to P-bodies and degraded by the enzymes contained therein through NANOS2-mediated deadenylation.

germ cells | P-body | meiosis

In the mouse, the primordial germ cells (PGCs) are segregated from the somatic cell lineage at an early gastrulation stage (1). Although the PGCs are potent producers of both oogonia and spermatogonia, sexual differentiation is induced after their colonization of the embryonic gonads with somatic cells. However, the initial steps leading to diversification of these cells have long remained unsolved. Retinoic acid (RA) signaling has recently been identified as the initial trigger for feminization (2). RA molecules derived from the mesonephros trigger meiotic initiation in female gonocytes via the induction of the RA responsive gene *Stra8*, which is required for premeiotic replication (3). In contrast, male gonocytes are protected from exposure to RA by CYP26B1, an RA metabolizing enzyme produced from somatic cells, resulting in the suppression of meiosis up to E13.5 (4, 5). In addition, *Nanos2* expression begins after E13.5 and is required for the maintenance and promotion of the male germ cell state (6).

Nanos is an evolutionarily conserved RNA-binding protein that is essential for germ cell development (7). In *Drosophila*, Nanos forms a complex with another RNA-binding protein, Pumilio, and represses the translation of the *hunchback*, *cyclin B*, and *hid* mRNAs thereby establishing embryonic polarity, mitotic quiescence, and suppression of apoptosis, respectively (8–10). Three *Nanos* homologs, *Nanos1–3*, exist in the mouse, among which *Nanos3* and *Nanos2* are expressed in the germ cells and are required to protect these cells from undergoing apoptosis during migration and after colonization of the male gonads, respectively (11, 12). In addition, *Nanos2* plays a key role during the sexual development of germ cells by suppressing meiosis and promoting male-type differentiation in the embryonic male gonads. Moreover, the forced expression of *Nanos2* in female gonocytes can induce the suppression of meiosis and promotion of male-type gene expression (6). However, the molecular mechanisms underlying how this protein accomplishes such pleiotropic functions in the mouse germ cells remain unknown.

In our present study, we find that NANOS2 localizes to P-bodies, a central hub of RNA degradation (13, 14). We further identify components of the CCR4-NOT deadenylation complex as NANOS2-associated proteins in vivo, which can cleave poly(A) RNA in vitro. We also show that specific mRNAs interact with NANOS2, and thus propose that NANOS2 plays a role in recruiting the CCR4-NOT deadenylation complex to trigger the degradation of specific RNAs.

Results

NANOS2 Localizes at P-Bodies During Gonocyte Development. To increase our understanding of the molecular mechanisms underlying the function of the NANOS2 protein, we first analyzed the cellular localization of this protein by immunostaining. Consistent with the results of our previous western analyses (15), NANOS2 protein was first detectable at E13.5 in the cytoplasm of male mouse gonocytes. This signal intensity increased until about E16.5 and then slightly decreased by E17.5. In addition, we found that some of the NANOS2 proteins formed discrete foci, the number of which gradually increased until E16.5 and then decreased thereafter (Fig. S1 *A–F*). Because *Drosophila* Vasa and Tudor are known to form cytoplasmic foci (16, 17), which are the polar granules in the germ plasm, we speculated that these NANOS2 foci might colocalize with the mouse homologs of Vasa, MVH (mouse vasa homolog) (18) and the Tudor protein TDRD1 (tudor domain containing 1) (19). However, these foci did not show any clear colocalization with NANOS2 (Fig. S2 *A–F*). We next tested the possibility that the NANOS2 foci might correspond to P-bodies, which are known to function as a center of RNA degradation. We thus conducted double-immunostaining using antibodies against the P-body components DCP2 and XRN1, an mRNA decapping enzyme and RNA exonuclease, respectively (13, 14). We were initially surprised to find that many P-bodies could be specifically observed only in germ cells and not in the somatic cells in E15.5 male gonads, and also that the NANOS2 foci clearly merged with those of DCP2 and XRN1 (Fig. 1 *A–F*) from E13.5 to E17.5 (Fig. S3 *A–F*). This suggests the possibility that NANOS2 may be involved in RNA degradation.

Nanos2 Functions in the Formation of P-Bodies. We further examined the status of the P-bodies in the mouse gonads of both sexes by immunostaining of p54/RCK, a homolog of *Drosophila* Me31B and also a marker of these structures (20). Although the P-bodies seemed to be present in the same number and size in the gonocytes of both sexes at E12.5, they were gradually reduced and eventually lost by E14.5 in female gonocytes (Fig. S4 *E* and *F*). In contrast, the P-bodies become much larger in both number and

Author contributions: A.S. and Y.S. designed research; A.S., performed research; K.I., K.. A., and J.K. analyzed data of microarray analyses; and A.S. and Y.S. wrote the paper.

The authors declare no conflict of interest.

This article is a PNAS Direct Submission.

[1]To whom correspondence should be addressed. E-mail: ysaga@lab.nig.ac.jp.

This article contains supporting information online at www.pnas.org/cgi/content/full/0908664107/DCSupplemental.

www.pnas.org/cgi/doi/10.1073/pnas.0908664107

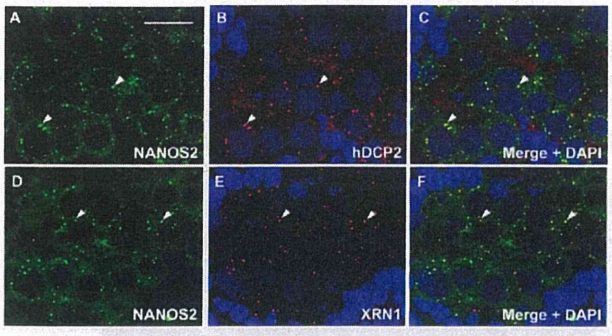

Fig. 1. NANOS2 localizes to the P-bodies in male mouse gonocytes. (*A–L*) Sections prepared from wild-type E15.5 male gonads were double-stained with mouse anti-NANOS2 (green) (*A* and *D*) and either hDCP2 (*B*) or mXRN1 (*E*) antibodies (red staining in each case). Arrowheads indicate colocalization of NANOS2 and hDCP2 (*C*) or XRN1 (*F*). DNA was counterstained with DAPI (blue). (Scale bar in *A*, 20 μm for all panels.)

size from E14.5, concomitant with the onset of NANOS2 expression, in male gonocytes (Fig. S4 *A–D*).

To further explore the role of NANOS2 in P-body formation, we examined the status of these structures in the absence of *Nanos2*. Although there were, somewhat unexpectedly, many P-bodies detected in both *Nanos2*$^{+/-}$ and *Nanos2*$^{-/-}$ male gonocytes at E13.5, their sizes became gradually larger, whereas their number became smaller, at the later stages of embryogenesis in the absence of *Nanos2* (Fig. 2*A–D*). This was also observed in *Nanos2, Bax* double-null male gonocytes (Fig. 2 *E* and *F*), where apoptotic cell death was suppressed, suggesting that apoptosis does not affect P-body status. This indicates that NANOS2 is not essential for the assembly of P-bodies but is required for the maintenance of their normal state. To further elucidate the functions of NANOS2 in P-body formation, we also examined the status of the P-bodies in NANOS2-expressing female gonocytes (6). Although they could not be detected in normal female gonocytes at E16.5, we found many P-bodies in NANOS2-expressing female cells and additionally observed that NANOS2 localizes at the P-bodies in these cells (Fig. 2 *G–I*). These data indicate that NANOS2 is sufficient to maintain the number of P-bodies when female gonocytes have acquired a male-type phenotype due to NANOS2 expression.

NANOS2 Interacts with the CCR4-NOT Deadenylation Complex and Regulates Its Localization. To explore the molecular functions of NANOS2, we searched for proteins that interact with it. To this end, we prepared male gonadal extracts from *Nanos2*$^{+/-}$ and *Nanos2*$^{-/-}$ embryos at E14.5 and subjected them to immunoprecipitation with anti-NANOS2 antibodies. We found that two major bands of more than 200 kDa were exclusively precipitated from *Nanos2*$^{+/-}$ gonads, and by mass spectrometric analysis identified these products as CNOT1, a component of the CCR4-NOT deadenylation complex (13) (Fig. 3A).

In further immunoprecipitation experiments, we used a transgenic mouse line expressing a FLAG-tagged NANOS2 under the direct control of the *Nanos2* enhancer (15) (Fig. S5*A*), since we had confirmed that this fusion protein was functional (Fig. S5 *B–F*) and localized at the P-bodies (Fig. S5 *G–I*). Western analyses revealed that CNOT1 coprecipitates with FLAG-tagged NANOS2 (Fig. 3*B, Upper*), confirming the results of our mass spectrometric analysis. We also found that other components of the CCR4-NOT complex, CNOT3, CNOT6L/Ccr4b, CNOT7/Caf1a, and CNOT9/Rcd1 (13, 21), also coprecipitated with FLAG-tagged NANOS2, indicating that NANOS2 associates with the CCR4-NOT deadenylation complex in vivo. We additionally found that this interaction is independent of RNA, as the levels of coprecipitated CNOT proteins were not affected by treatments with RNase (Fig. 3*B*). Finally, these CNOT proteins were found to colocalize with NANOS2 in P-bodies (Fig. 3 *C–E* and Fig. S6 *A–I*), suggesting that this complex may play a role in the activities of these elements.

To better understand the physiological significance of its interaction with NANOS2, we investigated the localization of CCR4-NOT deadenylation complex in *Nanos2*$^{-/-}$ male gonads by immunostaining CNOT proteins with DCP1A, another decapping enzyme and also a component of P-bodies (13, 14). Although CNOT3 was found to clearly localize to P-bodies in *Nanos2*$^{+/-}$ male gonads (Fig. 3 *F–H*), we detected only weak signals for this protein in P-bodies in the absence of NANOS2 (Fig. 3 *I–K*) even though the levels of CNOT3 are not reduced in *Nanos2*$^{-/-}$ male gonads (Fig. 3*L*). We obtained similar results for CNOT1 (Fig. S7). These data suggest that NANOS2 promotes the localization of the CCR4-NOT deadenylation complex to P-bodies, although a subpopulation of this complex still remains in these structures in the absence of NANOS2, possibly via a NANOS2-independent mechanism. Based on these findings and the fact that the CCR4-NOT deadenylation complex regulates the first step of mRNA degradation (22), we speculate that NANOS2 recruits this deadenylation complex to P-bodies where it promotes the degradation of RNAs.

Complex of NANOS2 and CCR4-NOT Deadenylation Complex in Male Germ Cells Retains Deadenylase Activity. To address the critical question of whether NANOS2-interacting deadenylase actually has catalytic activity, we used NANOS2-overexpressing (NANOS2 O/E) adult testes to obtain sufficient amounts of this protein and thus overcome the limitations of using embryonic testis in biochemical analyses. In the testis of the postnatal mouse, NANOS2 is expressed in a small population of undifferentiated spermatogonia (23) and localizes to P-bodies (Fig. S8 *A–C*) as in the male gonocytes. This expression is subsequently lost as these cells differentiate. However, if FLAG-tagged NANOS2 is forcedly and continuously expressed in the spermatogonial population, the male mouse become infertile because the spermatogonia remain in an undifferentiated state in the testis, in which a large number of NANOS2-positive spermatogonia occupy the periphery of the seminiferous tubules (23). In addition, FLAG-tagged NANOS2 also localizes to the P-bodies in the spermatogonia in the manner similar to endogenous Nanos2 (Fig. S8 *D–F*). We prepared testis extracts from this mouse and performed immunoprecipitations with anti-FLAG antibodies and control IgG, and then subjected these immunoprecipitates to in vitro deadenylase assay (21) (Fig. 4*A*). As shown in Fig. 4*B*, cleavage of the poly(A) RNA substrate occurred only with NANOS2 immunoprecipitates, which also contains the CNOT6L and CNOT7 catalytic components of the deadenylation complex (Fig. 4*C*). These results lead us to propose that NANOS2 promotes the degradation of NANOS2-interacting mRNAs through the deadenylase activity of the CCR4-NOT complex.

NANOS2 Interacts with Specific mRNAs and May Promote Their Degradation. Based on our working hypothesis, we further speculated that (*i*) the NANOS2 complex should contain specific mRNAs that would be degraded via NANOS2-mediated deadenylation, such that (*ii*) the expression levels of these transcripts would be low in wild-type male gonocytes but up-regulated in the absence of NANOS2. To test these possibilities, RNAs that coprecipitated with FLAG-tagged NANOS2 were purified and subjected to RT-PCR. Because we had previously shown that male gonocytes could enter meiosis in the absence of NANOS2, it was plausible that mRNAs involved in meiosis might be directly suppressed through NANOS2-mediated RNA degradation. As expected, *Sycp3*, *Stra8*, *Taf7l*, *Dazl*, and *Meisetz* (3, 24–27) transcripts that are implicated in meiosis were specifically detected only in the NANOS2 protein precipitates despite their very low expression in male gonads (Fig. 5 *A* and *B*). In contrast, the

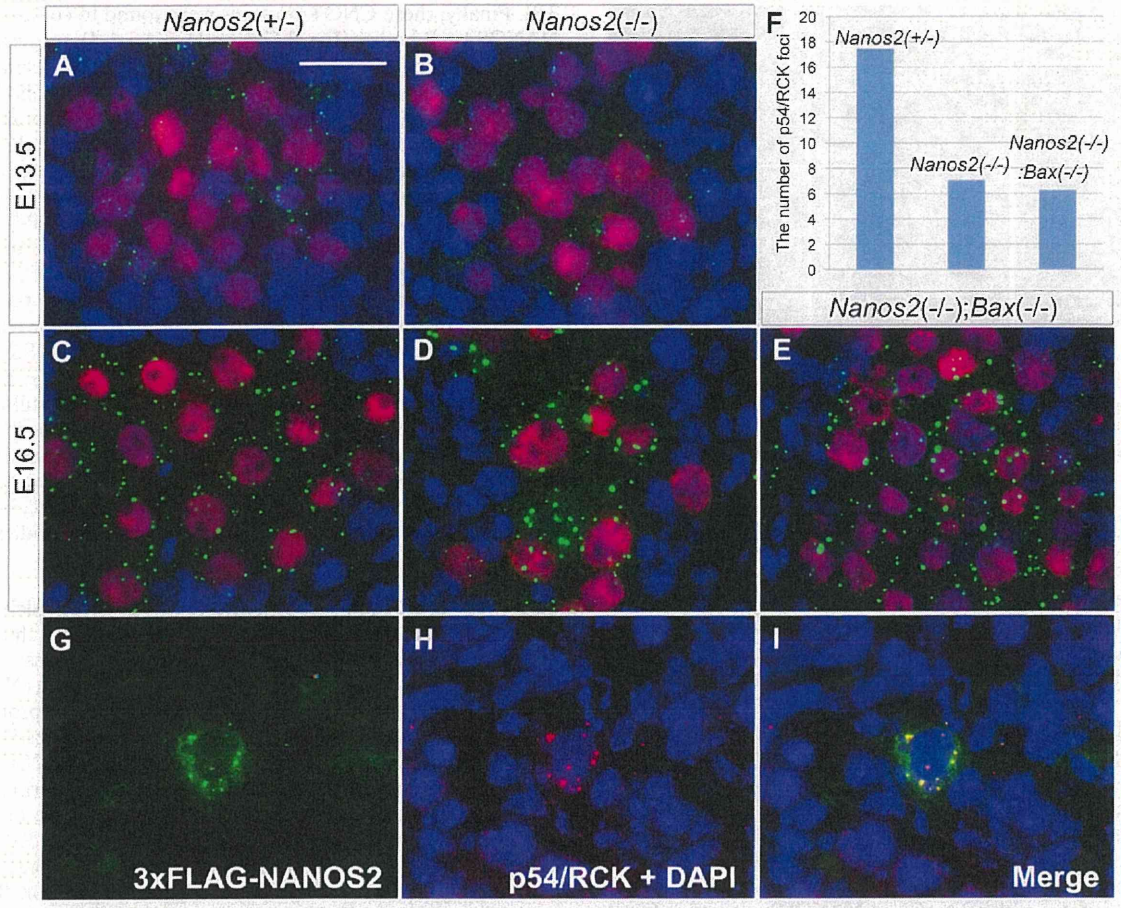

Fig. 2. Functional role of NANOS2 during the formation of the P-bodies. (*A–E*) Male gonadal sections from *Nanos2*$^{+/-}$ (*A* and *C*), *Nanos2*$^{-/-}$ (*B* and *D*), and *Nanos2*$^{-/-}$*Bax*$^{-/-}$ (*E*) embryos at stages E13.5 (*A* and *B*), and E16.5 (*C, D,* and *E*) were immunostained with p54/RCK (green) and TRA98 (red) antibodies. (*F*) Average number of p54/RCK foci per male gonocyte at E16.5 was quantified in each picture using ImageJ software (National Institutes of Health) and a cell counter, with the foci of less than a 20 permission value excluded using Photoshop (Adobe). The data shown correspond to two to three pictures. (*G–I*) A female gonadal section from a NANOS2-expressing embryo at E16.5 was immunostained with anti-FLAG (green) (*G*) and anti-p54/RCK (red) (*H*) antibodies. DNA was counterstained using DAPI (blue). (Scale bar in *A*, 20μm for *A–E* and *G–I*.)

G3pdh, *Dnmt3l* and *Dnmt3a* mRNAs did not show specific accumulation in the NANOS2 precipitates although they are all highly expressed in male gonads. These data indicate that the mRNAs involved in meiosis specifically interact with NANOS2 in vivo.

We next investigated global changes in gene expression upon the loss of *Nanos2* using comparative GeneChip analyses (Table S1). The resulting scatter plots showed that many genes become up- or down-regulated in *Nanos2*$^{-/-}$ male gonads by E15.5 (Fig. S9 *A–C*). For example, we found that the genes highly expressed only in male gonocytes, such as *Dnmt3l*, *Tdrd1* and *Miwi2*/*Piwi-like 4* (19, 28, 29), are down-regulated in the *Nanos2*$^{-/-}$ male gonads, whereas *Figla*, *Lhx8* and *Nobox*, which have been shown to be essential only for oogenesis and not for spermatogenesis (30–32), become accumulated in the *Nanos2*$^{-/-}$ male gonads (6) (Fig. S9 *D–I*). These results suggest that male gonocytes cannot enter the male pathways and become feminized by the up-regulation of female-type genes. In addition, and consistent with the results of our immunoprecipitation assay, *Sycp3*, *Stra8*, *Taf7l*, *Dazl*, and *Meisetzs* mRNAs were also found to be up-regulated in *Nanos2*$^{-/-}$ male gonads (Fig. 5 *C–G*). Our current findings thus indicate that NANOS2-interacting mRNAs become accumulated if NANOS2 is absent in male gonocytes, which in turn indicates that NANOS2 might be indirectly affecting the transcription of these genes, or that they are normally suppressed in wild-type male gonocytes through a NANOS2-directed mechanism, possibly a deadenylation pathway.

Discussion

Molecular Role of NANOS2. In our current study, we show that the CCR4-NOT deadenylation complex is coprecipitated with NANOS2 from male gonadal extracts. This is the first evidence that the interaction between a Nanos homolog and the CCR4-NOT deadenylation complex exists *in vivo,* although it has been shown using a yeast two-hybrid system that *Drosophila* Nanos can directly and potently bind to NOT4, a component of the CCR4-NOT complex (33). Hence, as suggested previously by Kadyrova et al. for *Drosophila* Nanos, and as confirmed by our present analyses in vivo, the recruitment of the CCR4-NOT deadenylation complex to target mRNAs may be a conserved function of the Nanos proteins.

We also found that NANOS2 localizes to P-bodies in the male gonocytes and adult mouse spermatogonia. P-bodies are known to be a central hub of RNA degradation, in which decapping enzymes and exonucleases are also localized. However, emerging evidence in other systems suggests that P-bodies not only function to degrade RNAs but also to store mRNAs in a translationally quiescent state until needed (13). In addition, *Drosophila* Nanos promotes the deadenylation of poly(A) tail in *hunchback* mRNA and represses its translation without changing the mRNA level

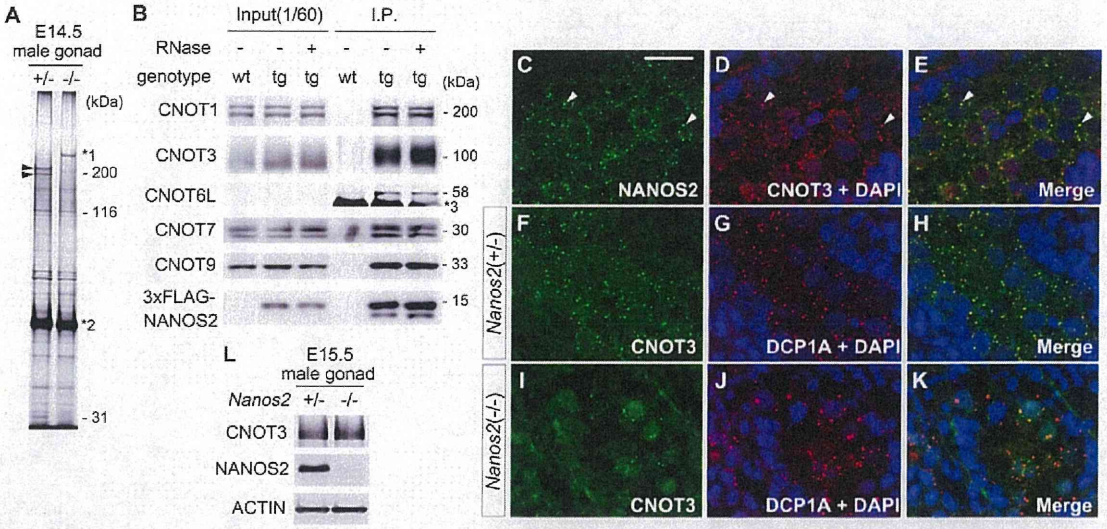

Fig. 3. Interaction between NANOS2 and the CCR4-NOT deadenylation complex. (*A*) Proteins coimmunoprecipitated with NANOS2 from E14.5 wild-type (lane 1) and *Nanos2*$^{-/-}$ (lane 2) male gonadal extracts using rabbit anti-NANOS2 antibodies. Arrowheads indicate CNOT1. *1, nonspecific band; *2, IgG polypeptide. (*B*) Immunoprecipitation–Western blot analyses of proteins from male gonadal extracts of wild-type and transgenic embryos expressing 3×FLAG-NANOS2. *3, IgG polypeptide from the anti-FLAG antibody. (*C–E*) Male gonadal sections from E15.5 embryos were immunostained with mouse NANOS2 (green) (*C*) and CNOT3 (red) (*D*) antibodies. Arrowheads in *C–E* indicate colocalization between NANOS2 and CNOT3. (*F–K*) Male gonadal sections from *Nanos2*$^{+/-}$ (*F–H*) and *Nanos2*$^{-/-}$ (*I–K*) embryos at E15.5 were immunostained with DCP1A (red) (*G* and *J*) and CNOT3 (green) (*F* and *I*) antibodies. DNA was labeled via DAPI counterstaining (blue). (*L*) Western blot analyses of proteins from the male gonads of *Nanos2*$^{+/-}$ and *Nanos2*$^{-/-}$ embryos at E15.5.

(34). We cannot therefore rule out the possibility that NANOS2 not only promotes the degradation of mRNAs involved in meiosis but also retains other transcripts at P-bodies to sequester them in a translationally inactive state during embryogenesis. These transcripts may be released from the P-bodies and translated to promote differentiation after birth as NANOS2 expression begins to disappear.

P-Body Formation in Male Mouse Gonocytes. P-bodies have been well characterized in yeast and mammalian cultured cells, and the in vivo status of these foci has begun to be described recently also in worms and flies (35–38). We found from our current analyses that P-bodies are specifically formed and/or maintained in the germ cells of male mouse embryonic gonads, whereas no such structures are detectable in somatic cells. Furthermore, female mouse gonocytes fail to maintain P-bodies at later stages of embryogenesis. We thus suggest that P-bodies play roles in cell-type specific differentiation during mouse development through RNA metabolism.

It has also been shown that P-bodies are dynamic structures and that their size and number reflects the status of the mRNA supply. If the transit of mRNAs into the P-bodies is inefficient, the size and number of these structures becomes extremely small. In contrast, they become larger when the mRNA decapping pathway is blocked (39, 40). Furthermore, it has been recently reported that deadenylation is required for P-body formation (41). Taking into account the data presented in these earlier reports and our current model, P-bodies would be expected to be small in *Nanos2*$^{-/-}$ male gonocytes because the mRNA supply to these structures and subsequent deadenylation efficiency would be inhibited in the absence of NANOS2. However, we were surprised to find that the sizes of the P-bodies

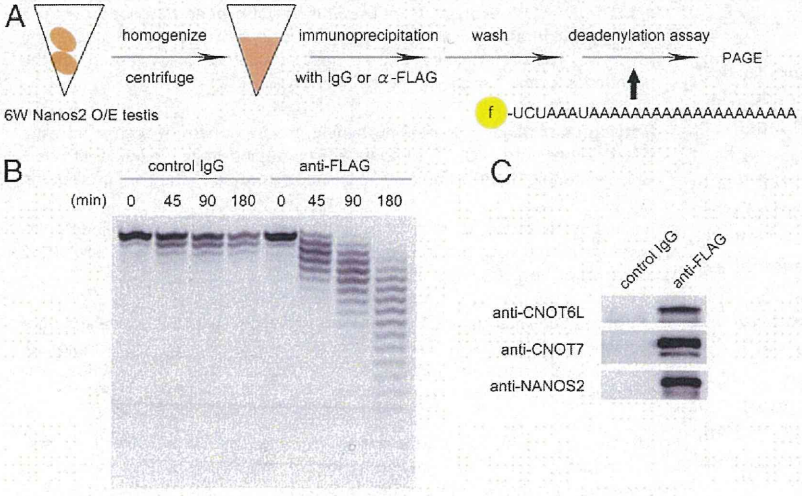

Fig. 4. The protein complex of NANOS2 and CCR4-NOT complex has in vitro deadenylase activity. (*A*) Schematic representation of the in vitro deadenylase assay method using NANOS2 over-expressing (O/E) testes. (*B*) FLAG-tagged NANOS2 was precipitated with anti-FLAG antibodies from the testis extracts of a 6-week-old NANOS2 O/E mouse and incubated with 5′-fluorescein isothiocyanate-labeled poly (A) RNA substrate for 0, 45, 90, and 180 min. Samples were then analyzed on a denaturing sequencing gel, as previously described (**21**) (*G*). (*C*) Western blot analyses reveaing that CNOT6L and CNOT7 are coprecipitated with FLAG-tagged NANOS2.

DEVELOPMENTAL BIOLOGY

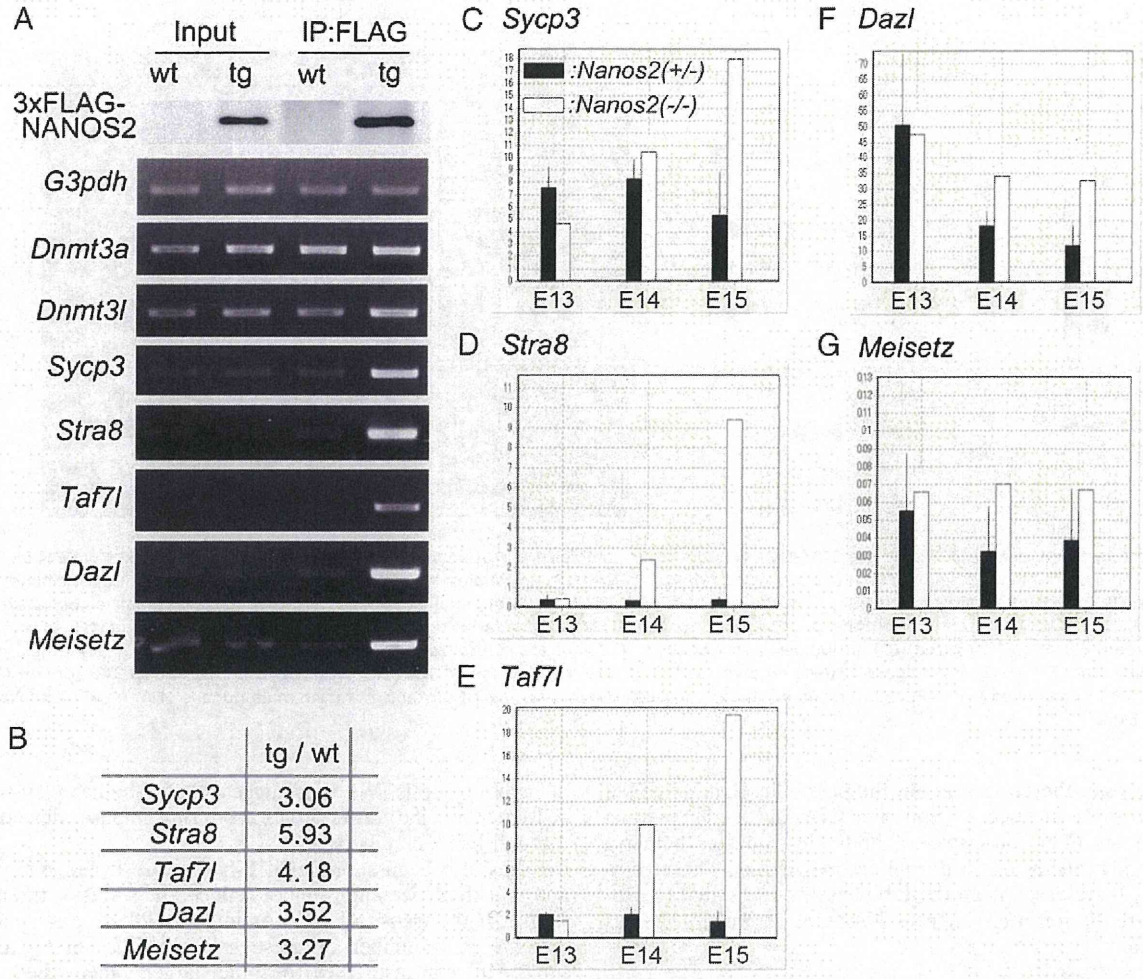

B

	tg / wt
Sycp3	3.06
Stra8	5.93
Taf7l	4.18
Dazl	3.52
Meisetz	3.27

Fig. 5. NANOS2 interacts with specific mRNAs and may promote their degradation. (*A*) Male gonadal extracts from wild-type (*wt*) and transgenic (*tg*) mice expressing FLAG-NANOS2 at E15.5 were subjected to immunoprecipitation (IP) with FLAG antibodies. RNA precipitates were analyzed by semi-quantitative RT-PCR. (*B*) Quantification of each mRNA enrichment from a FLAG IP of *tg* extracts using real-time RT-PCR. Fold enrichment of each mRNA coprecipitated from *tg* compared with those from *wt* is indicated. Mean value of three independent QRT-PCR results is shown. (*C–G*) Expression profiling of the *Sycp3* (*C*), *Stra8* (*D*), *Taf7l* (*E*), *Dazl* (*F*), and *Meisetz* (*G*) genes in male gonads from *Nanos2*$^{+/-}$ and *Nanos2*$^{-/-}$ embryos at E13.5-E15.5 using the Affymetrix GeneChip System as previously described (43) (*X*-axis; embryonic stage, *Y*-axis; expression level, black bars; *Nanos2*$^{+/-}$ embryos, white bars; *Nanos2*$^{-/-}$ embryos).

became larger in this biological context, although their number was decreased. These data thus indicate that male gonocytes have a unique program for P-body formation that occurs both in a NANOS2-dependent and -independent manner.

mRNAs Targeted by NANOS2. We elucidated that the protein complex of NANOS2 and CCR4-NOT complex has deadenylase activity in vitro. We thus expected that the poly(A) tail lengths of NANOS2-interacting mRNAs would be maintained without NANOS2. To test this scenario, we assayed the poly(A) tail length of NANOS2-interacting mRNAs. However, we could not observe clear shortening of the poly(A) tail in wild-type male gonads, possibly because of their low abundance. New experimental systems will be required in the future to address this issue.

On the other hand, it was noteworthy that we identified *Stra8* as a NANOS2-interacting mRNA because we have shown previously that *Stra8* is up-regulated at the transcriptional level in *Nanos2*$^{-/-}$ male gonocytes (6). These data together indicate that the suppression of *Stra8* in male gonocytes is ensured at both the transcriptional and translational levels, suggesting the critical functional importance of suppressing this gene during male gonocyte development.

Materials and Methods

Mice. Both the *Nanos2* and *Bax*-knockout mouse lines and PCR methods used for the verification of each mutant allele have been previously described (11, 42). The NANOS2-expressing mouse line has also been described (23) The transgene containing 3×FLAG-tagged *Nanos2* with the 3′-UTR under the control of Nanos2 enhancer (9.2 kb upstream sequence) was used for the production of the transgenic mouse line.

Histological Methods. For immunostaining, mouse gonads of both sexes were directly embedded in O.C.T. compound (Sakura) and frozen in liquid nitrogen. After sectioning (8 μm), samples were stained according to standard procedures.

Immunoprecipitation. Extracts of male gonads from E14.5 or E15.5 embryos were incubated with protein-A beads crosslinked with rabbit anti-NANOS2 antibody or anti-FLAG M2 affinity gel (Sigma).

In Vitro Deadenylase Assay. The testis extracts from NANOS2-expressing mice were incubated with anti-FLAG M2 affinity gel or Mouse IgG-agarose (Sigma). After several washes, precipitates were then subjected to a deadenylase assay as previously described (21).

RT-PCR. After synthesis of first-strand cDNAs with SuperScript III reverse transcriptase and $(dT)_{20}$ primer (Invitrogen), PCR analyses were carried out either using a regular or real-time protocol.

GeneChip Analysis. Total RNAs were purified from cells corresponding to the male gonads of *Nanos2-LacZ* knock-in heterozygous and homozygous embryos, and analyzed using a GeneChip Mouse Genome 430 2.0 Array (Affymetrix).

Details of the methods and primer sequences used for each section are provided in *SI Text.*

ACKNOWLEDGMENTS. We thank the following researchers for generously providing antibodies: Y. Nishimune (TRA98), S. Chuma and N. Nakatsuji (anti-TDRD1), T. Noce (anti-MVH), M. Kiledjian (anti-hDCP2), W. D. Heyer (anti-mXRN1), H. T. Timmers (anti-CNOT1), T. Tamura (anti-CNOT3), T. Yamamoto (anti-CNOT6L/Ccr4b), A. B. Shyu (anti-CNOT7/Caf1a), and H. Okayama (anti-CNOT9/Rcd1). We are also very grateful to M. Morita and T. Yamamoto for their technical advice and assistance with the *in vitro* deadenylase assay. We further thank Noriko Moriyama for technical assistance with the microarray experiments and Yuki Nakajima for help with the histological analyses. This work was partly supported by Grants-in-Aid for National BioResource Project and of the Genome Network Project of the Ministry of Education, Culture, Sports, Science and Technology, Japan.

1. Hayashi K, de Sousa Lopes SM, Surani MA (2007) Germ cell specification in mice. *Science* 316:394–396.
2. Bowles J, Koopman P (2007) Retinoic acid, meiosis and germ cell fate in mammals. *Development* 134:3401–3411.
3. Baltus AE, et al. (2006) In germ cells of mouse embryonic ovaries, the decision to enter meiosis precedes premeiotic DNA replication. *Nat Genet* 38:1430–1434.
4. Bowles J, et al. (2006) Retinoid signaling determines germ cell fate in mice. *Science* 312:596–600.
5. Koubova J, et al. (2006) Retinoic acid regulates sex-specific timing of meiotic initiation in mice. *Proc Natl Acad Sci USA* 103:2474–2479.
6. Suzuki A, Saga Y (2008) Nanos2 suppresses meiosis and promotes male germ cell differentiation. *Genes Dev* 22:430–435.
7. Kobayashi S, Yamada M, Asaoka M, Kitamura T (1996) Essential role of the posterior morphogen nanos for germline development in Drosophila. *Nature* 380:708–711.
8. Murata Y, Wharton RP (1995) Binding of pumilio to maternal hunchback mRNA is required for posterior patterning in Drosophila embryos. *Cell* 80:747–756.
9. Asaoka-Taguchi M, Yamada M, Nakamura A, Hanyu K, Kobayashi S (1999) Maternal Pumilio acts together with Nanos in germline development in Drosophila embryos. *Nat Cell Biol* 1:431–437.
10. Sato K, et al. (2007) Maternal Nanos represses hid/skl-dependent apoptosis to maintain the germ line in Drosophila embryos. *Proc Natl Acad Sci USA* 104:7455–7460.
11. Tsuda M, et al. (2003) Conserved role of nanos proteins in germ cell development. *Science* 301:1239–1241.
12. Suzuki H, Tsuda M, Kiso M, Saga Y (2008) Nanos3 maintains the germ cell lineage in the mouse by suppressing both Bax-dependent and -independent apoptotic pathways. *Dev Biol* 318:133–142.
13. Parker R, Sheth U (2007) P bodies and the control of mRNA translation and degradation. *Mol Cell* 25:635–646.
14. Eulalio A, Behm-Ansmant I, Izaurralde E (2007) P bodies: At the crossroads of post-transcriptional pathways. *Nat Rev Mol Cell Biol* 8:9–22.
15. Suzuki A, Tsuda M, Saga Y (2007) Functional redundancy among Nanos proteins and a distinct role of Nanos2 during male germ cell development. *Development* 134:77–83.
16. Hay B, Ackerman L, Barbel S, Jan LY, Jan YN (1988) Identification of a component of Drosophila polar granules. *Development* 103:625–640.
17. Bardsley A, McDonald K, Boswell RE (1993) Distribution of tudor protein in the Drosophila embryo suggests separation of functions based on site of localization. *Development* 119:207–219.
18. Toyooka Y, et al. (2000) Expression and intracellular localization of mouse Vasa-homologue protein during germ cell development. *Mech Dev* 93:139–149.
19. Chuma S, et al. (2003) Mouse Tudor Repeat-1 (MTR-1) is a novel component of chromatoid bodies/nuages in male germ cells and forms a complex with snRNPs. *Mech Dev* 120:979–990.
20. Kedersha N, Anderson P (2007) Mammalian stress granules and processing bodies. *Methods Enzymol* 431:61–81.
21. Morita M, et al. (2007) Depletion of mammalian CCR4b deadenylase triggers elevation of the p27Kip1 mRNA level and impairs cell growth. *Mol Cell Biol* 27: 4980–4990.
22. Meyer S, Temme C, Wahle E (2004) Messenger RNA turnover in eukaryotes: Pathways and enzymes. *Crit Rev Biochem Mol Biol* 39:197–216.
23. Sada A, Suzuki A, Suzuki H, Saga Y (2009) The RNA-binding protein NANOS2 is required to maintain murine spermatogonial stem cells. *Science* 325:1394–1398.
24. Yuan L, et al. (2000) The murine SCP3 gene is required for synaptonemal complex assembly, chromosome synapsis, and male fertility. *Mol Cell* 5:73–83.
25. Cheng Y, et al. (2007) Abnormal sperm in mice lacking the Taf7l gene. *Mol Cell Biol* 27:2582–2589.
26. Ruggiu M, et al. (1997) The mouse Dazla gene encodes a cytoplasmic protein essential for gametogenesis. *Nature* 389:73–77.
27. Hayashi K, Yoshida K, Matsui Y (2005) A histone H3 methyltransferase controls epigenetic events required for meiotic prophase. *Nature* 438:374–378.
28. Sakai Y, Suetake I, Shinozaki F, Yamashina S, Tajima S (2004) Co-expression of de novo DNA methyltransferases Dnmt3a2 and Dnmt3L in gonocytes of mouse embryos. *Gene Expr Patterns* 5:231–237.
29. Aravin AA, et al. (2008) A piRNA pathway primed by individual transposons is linked to de novo DNA methylation in mice. *Mol Cell* 31:785–799.
30. Soyal SM, Amleh A, Dean J (2000) FIGalpha, a germ cell-specific transcription factor required for ovarian follicle formation. *Development* 127:4645–4654.
31. Choi Y, Ballow DJ, Xin Y, Rajkovic A (2008) Lim homeobox gene, lhx8, is essential for mouse oocyte differentiation and survival. *Biol Reprod* 79:442–449.
32. Rajkovic A, Pangas SA, Ballow D, Suzumori N, Matzuk MM (2004) NOBOX deficiency disrupts early folliculogenesis and oocyte-specific gene expression. *Science* 305: 1157–1159.
33. Kadyrova LY, Habara Y, Lee TH, Wharton RP (2007) Translational control of maternal Cyclin B mRNA by Nanos in the Drosophila germline. *Development* 134:1519–1527.
34. Wreden C, Verrotti AC, Schisa JA, Lieberfarb ME, Strickland S (1997) Nanos and pumilio establish embryonic polarity in Drosophila by promoting posterior deadenylation of hunchback mRNA. *Development* 124:3015–3023.
35. Boag PR, Atalay A, Robida S, Reinke V, Blackwell TK (2008) Protection of specific maternal messenger RNAs by the P body protein CGH-1 (Dhh1/RCK) during Caenorhabditis elegans oogenesis. *J Cell Biol* 182:543–557.
36. Gallo CM, Munro E, Rasoloson D, Merritt C, Seydoux G (2008) Processing bodies and germ granules are distinct RNA granules that interact in C. elegans embryos. *Dev Biol* 323:76–87.
37. Noble SL, Allen BL, Goh LK, Nordick K, Evans TC (2008) Maternal mRNAs are regulated by diverse P body-related mRNP granules during early Caenorhabditis elegans development. *J Cell Biol* 182:559–572.
38. Lee L, Davies SE, Liu JL (2009) The spinal muscular atrophy protein SMN affects Drosophila germline nuclear organization through the U body-P body pathway. *Dev Biol* 332:142–155.
39. Sheth U, Parker R (2003) Decapping and decay of messenger RNA occur in cytoplasmic processing bodies. *Science* 300:805–808.
40. Eulalio A, Behm-Ansmant I, Schweizer D, Izaurralde E (2007) P-body formation is a consequence, not the cause, of RNA-mediated gene silencing. *Mol Cell Biol* 27: 3970–3981.
41. Zheng D, et al. (2008) Deadenylation is prerequisite for P-body formation and mRNA decay in mammalian cells. *J Cell Biol* 182:89–101.
42. Knudson CM, Tung KS, Tourtellotte WG, Brown GA, Korsmeyer SJ (1995) Bax-deficient mice with lymphoid hyperplasia and male germ cell death. *Science* 270: 96–99.
43. Kanno J, et al. (2006) "Per cell" normalization method for mRNA measurement by quantitative PCR and microarrays. *BMC Genomics* 7:64.

Visualization of omics data for systems biology

Nils Gehlenborg[1,2], Seán I O'Donoghue[3], Nitin S Baliga[4], Alexander Goesmann[5], Matthew A Hibbs[6], Hiroaki Kitano[7–9], Oliver Kohlbacher[10], Heiko Neuweger[5], Reinhard Schneider[3], Dan Tenenbaum[4] & Anne-Claude Gavin[3]

High-throughput studies of biological systems are rapidly accumulating a wealth of 'omics'-scale data. Visualization is a key aspect of both the analysis and understanding of these data, and users now have many visualization methods and tools to choose from. The challenge is to create clear, meaningful and integrated visualizations that give biological insight, without being overwhelmed by the intrinsic complexity of the data. In this review, we discuss how visualization tools are being used to help interpret protein interaction, gene expression and metabolic profile data, and we highlight emerging new directions.

Visualization has long been key in helping to understand biological systems, such as metabolism[1], signaling[2] and the regulation of gene expression[3]. In recent years, the study of such systems has been profoundly influenced by the development of a wide range of high-throughput experimental methods (**Box 1**), resulting in a greatly increased volume of complex, interconnected data. Remarkably, in spite of these changes, and in spite of the development of new methods for visualizing and analyzing these data, we still use the same primary visual metaphor to communicate ideas about biological systems: namely, pathways (graphs that show overall changes in state) or, more generally, networks (graphs that do not necessarily show state changes).

As high-throughput experimental methods have become more routine, many more scientists are using network and pathway visualization to record and communicate their findings. There are now over 300 web resources[4] (see http://pathguide.org/) providing access to many thousands of pathways and networks that document millions of interactions between proteins, genes and small molecules.

There has been a corresponding increase in the development of visualization tools for systems biology data[5–7]. These tools are very diverse, but they can be broadly divided into two partly overlapping categories, the first consisting of tools focused on automated methods for interpreting and exploring large biological networks (**Table 1**), and the second consisting of tools focused on assembly and curation of pathways (**Table 2**). Many of these tools are tightly integrated with public databases, thus allowing users to visualize and interpret their own data in the context of previous knowledge.

For users and developers of these visualization tools, one of the key challenges is how to benefit from the explosion in systems biology data without being overwhelmed by it—or, in practical terms, how to present the data at the right level of detail, in a cohesive, insightful manner. Clearly, the answers depend on context.

In this review, we first discuss the methods and tools now being used to visualize and analyze data sets from three main types of high-throughput experiments: namely, the investigation of protein-protein interactions, of gene expression profiles and of metabolic profiles. Such experiments are used to study cellular response to a wide variety of conditions—including drug exposure, disease states and specific genetic

[1]European Bioinformatics Institute, Cambridge, UK. [2]Graduate School of Life Sciences, University of Cambridge, Cambridge, UK. [3]European Molecular Biology Laboratory, Heidelberg, Germany. [4]Institute for Systems Biology, Seattle, Washington, USA. [5]CeBiTec, Bielefeld University, Bielefeld, Germany. [6]The Jackson Laboratory, Bar Harbor, Maine, USA. [7]Sony Computer Science Laboratories, Tokyo, Japan. [8]The Systems Biology Institute, Tokyo, Japan. [9]Okinawa Institute of Science and Technology, Okinawa, Japan. [10]University of Tübingen, Tübingen, Germany. Correspondence should be addressed to S.I.O. (sean.odonoghue@embl.de).

PUBLISHED ONLINE 1 MARCH 2010; DOI:10.1038/NMETH.1436